CATKE: a turbulent-kinetic-energy-based parameterization for ocean microturbulence with dynamic convective adjustment

Gregory LeClaire Wagner[1], Adeline Hillier[1], Navid C. Constantinou[2], Simone Silvestri[1], Andre Souza[1], Keaton Burns[1], Ali Ramadhan[1], Chris Hill[1], Jean-Michel Campin[1], John Marshall[1], and Raffaele Ferrari[1]

[1]Massachusetts Institute of Technology, Cambridge, MA, USA
[2]Australian National University, Canberra, Australia

Key Points:

- We describe a new diffusive parameterization for ocean microturbulence based on convective adjustment and turbulent kinetic energy.
- CATKE uses a dynamic convective mixing length to efficiently and accurately model the rate of convective mixing.
- We calibrate and assess CATKE using thirty idealized large eddy simulations.

Corresponding author: Gregory L. Wagner, mailto:wagner.greg@gmail.comwagner.greg@gmail.com

Abstract

We describe CATKE, a parameterization for ocean microturbulence with scales between 1 and 100 meters. CATKE is a one-equation model that predicts diffusive turbulent vertical fluxes a prognostic turbulent kinetic energy (TKE) and a diagnostic mixing length that features a dynamic model for convective adjustment (CA). With its convective mixing length, CATKE predicts not just the depth range where microturbulence acts but also the timescale over which mixing occurs, an important aspect of turbulent convection not captured by convective adjustment schemes. As a result, CATKE can describe the competition between convection and other processes such as baroclinic restractification or biogeochemical production-destruction. We estimate CATKE's free parameters with *a posteriori* calibration to eighteen large eddy simulations of the ocean surface boundary layer, and validate CATKE against twelve additional large eddy simulations with stronger and weaker forcing than used during calibration. We find that a CATKE-parameterized single column model accurately predicts the depth structure of buoyancy and momentum at vertical resolutions between 2 and 16 meters and with time steps of 10-20 minutes. We propose directions for future model development, and future efforts to recalibrate CATKE's parameters against more comprehensive and realistic datasets.

Plain Language Summary

Turbulence is everywhere in the Earth's ocean, from ephemeral swirls no bigger than a fingertip to gigantic eddies larger than Iceland. Ocean models simulate ocean currents by dividing the ocean into "grid cells" between 10 and 100 kilometers wide. As a result, ocean models do a pretty good job simulating eddies that are significantly larger than a single grid cell. But models do a far worse job incorporating the effects of eddies that are roughly person- to building-sized, and thus smaller than a grid cell. This is a problem because these small yet mighty eddies mix heat and carbon deep into the ocean, and thus help keep the atmosphere from getting too hot, and too rich in CO_2. In this paper we propose a new model component called "CATKE" (pronounced *kăt-kee*) that does a pretty good job at incorporating the effect of such relatively small ocean eddies in climate models. CATKE stands for "Convective Adjustment and Turbulent Kinetic Energy". Basically, CATKE keeps track of the *energy* of small-scale turbulence — a measure of how vigorous it is, and thus how much it mixes the ocean — to predict ocean mixing rates. We hope CATKE helps us make more accurate climate predictions.

1 Introduction

Vertical mixing by ocean microturbulence with scales between 1 and 100 meters is an important process affecting, for example, ocean uptake of atmospheric heat and carbon (Price et al., 1986; Large et al., 1994; Omand et al., 2015), the structure of the ocean interior (Luyten et al., 1983; Williams, 1991), and ocean circulation on decadal to millennial time-scales. In large-scale ocean models — from regional models covering tens of kilometers to global ocean models —microturbulent vertical fluxes are approximately modeled by *parameterizations*. Imperfect predictions by microturbulence parameterizations can affect the accuracy of ocean and climate predictions, contributing, for example, to biases in Southern Ocean mixed layer depth (Sallée et al., 2013; DuVivier et al., 2018), tropical sea surface temperature (G. Li & Xie, 2014), and water mass formation (Groeskamp et al., 2019).

Ocean microturbulence parameterizations for climate prediction are biased not just because microturbulence is challenging to model, but also because of severe restrictions on model formulation imposed by the computational costs of climate modeling. Consider "two-equation" parameterizations like k–ϵ (Umlauf & Burchard, 2003; Mellor & Yamada, 1982; Harcourt & D'Asaro, 2008), which estimate turbulent diffusivities for momentum and tracers by evolving turbulent kinetic energy (TKE) together with a second auxiliary variable like TKE dissipation ϵ. Two-equation parameterizations are widely used in both regional ocean

simulations and aerodynamics and may be considered a gold standard for microturbulence parameterization — but are rarely used for global ocean climate modeling. The reason is that reliable predictions with two-equation models for typical oceanic conditions require time steps shorter than 6 minutes (Reffray et al., 2015; Reichl & Hallberg, 2018), much shorter than the 15–120 minute time steps required for typical current climate applications.

In this paper we describe a new one-equation microturbulence parameterization designed for climate application called "CATKE" featuring a dynamic convective adjustment (CA) model and a budget for turbulent kinetic energy (TKE). Like existing one-equation parameterizations widely used in European climate models (Gaspar et al., 1990; Blanke & Delecluse, 1993; Kuhlbrodt et al., 2018; Madec et al., 2017; Gutjahr et al., 2021; Jungclaus et al., 2022), CATKE predicts downgradient, diffusive momentum and tracer transport through effective turbulent diffusivities in terms of a prognostic TKE variable and a diagnostic mixing length scale model.

CATKE's formulation is described in section 2. One of the strengths that CATKE shares with other one-equation parameterizations is a skillful formulation for the shear turbulence length scale introduced in section 2.1.1. Yet this shear turbulence length scale "has no meaning" (Blanke & Delecluse, 1993) in convective conditions. Convection, perhaps the most important oceanic microturbulent process, controls the wintertime mixed layer depth outside the tropics and plays an important role in the meridional overturning circulation. Current one-equation parameterizations (Madec et al., 2017; Gutjahr et al., 2021; Jungclaus et al., 2022) use a constant "convective adjustment" diffusivity typically around $\kappa_c = 0.1\,\mathrm{m^2\,s^{-1}}$. A constant convective adjustment diffusivity is problematic, however, because a constant diffusivity cannot accurately describe the *rate* of convective mixing — which varies both with boundary layer depth and the intensity of the destabilizing surface buoyancy flux — across the wide range of convective conditions realized in Earth's ocean. One of the main contribution of this paper is the new convective length scale parameterization for TKE-based models, described in section 2.1.2, that predicts the convective diffusivity and thus the rate of convective mixing based on a dimensional analysis due to Deardorff et al. (1970).

CATKE has 18 free parameters, commensurate with typical ocean microscale parameterizations. (Most parameterizations have O(10) parameters, though free parameters are rarely enumerated. We count 16-17 for the K-profile-parameterization through a close reading of Large et al. (1994), ≈ 10 for NEMO's TKE-based parameterization based on Madec et al. (2017), and infer that two equation models have between 6–12 free parameters based on (Burchard & Bolding, 2001) and (Mellor & Yamada, 1982).) In section 3, we calibrate CATKE's free parameters against 18 idealized large eddy simulations (LES) of ocean surface boundary layer mixing, and use 12 additional LES for validation. Our LES are categorized by forcing "magnitude" into suites of six scenarios each: *(i)* free convection, *(ii)* wind-forced without rotation, *(iii)* wind-forced with rotation, and three cases *(iv–vi)* with combinations of convective and wind-forced turublence, with rotation. All LES use a rectangular domain 512^2 meters square and 256 meters deep, and all are initialized from rest with a depth-dependent buoyancy profile whose buoyancy frequency varies between between 10^{-6}–$10^{-5}\,\mathrm{s^{-2}}$. The wind-forced LES model surface waves using a wind-wave equilibrium model with a peak wave number chosen to produce $\mathrm{La} = 0.3$, the peak of the global distribution of La (Belcher et al., 2012). We use three suites for calibration involving 12, 24, and 48 hours of simulation, at which point all 18 simulations have roughly the same boundary layer depth. The two validation suites are run for 6 and 72 hours, thus possessing stronger and weaker forcing than used for calibration. The LES are described in more detail in Appendix A.

Our calibration uses Ensemble Kalman Inversion (Iglesias et al., 2013) to solve an inverse problem for the free parameters that minimize the mismatch between the 18 calibration LES coarse grained to both 4- and 8-meter resolution, and corresponding sets of CATKE-parameterized single column simulations using a 20 minute time step. Our calibration framework is therefore "*a posteriori*" (Duraisamy, 2021; Frezat et al., 2022; Ramadhan et al., 2022) and incorporates numerical errors and discrete implementation details, which helps

ensure that CATKE-parameterized numerical solutions are stable and reliable. We validate CATKE's skill in the same single column setting at three resolutions with 2-, 8- and 16-meter spacing. We find that CATKE delivers accurate and reliable predictions for boundary layer scenarios for all resolutions and with 20 minute time steps. Side-by-side LES and CATKE predictions are shown in figure 1.

We explore CATKE's dynamics in more diverse ocean mixing scenarios in section 4, including boundary layers forced by diuranlly-varying forcing, mixing by turbulence produced by an external source, and mixing in forced stratified shear turbulence. We conclude in section 5 with comments about future efforts to calibrate CATKE to more comprehensive data sets and future model development efforts to capture physics not considered in this work, such as the effect of surface wave fields that vary independently from winds. The most important piece of future work is the construction of a global calibration context that will permit to further calibrate CATKE's free parameters from satellite and in-situ ocean observations.

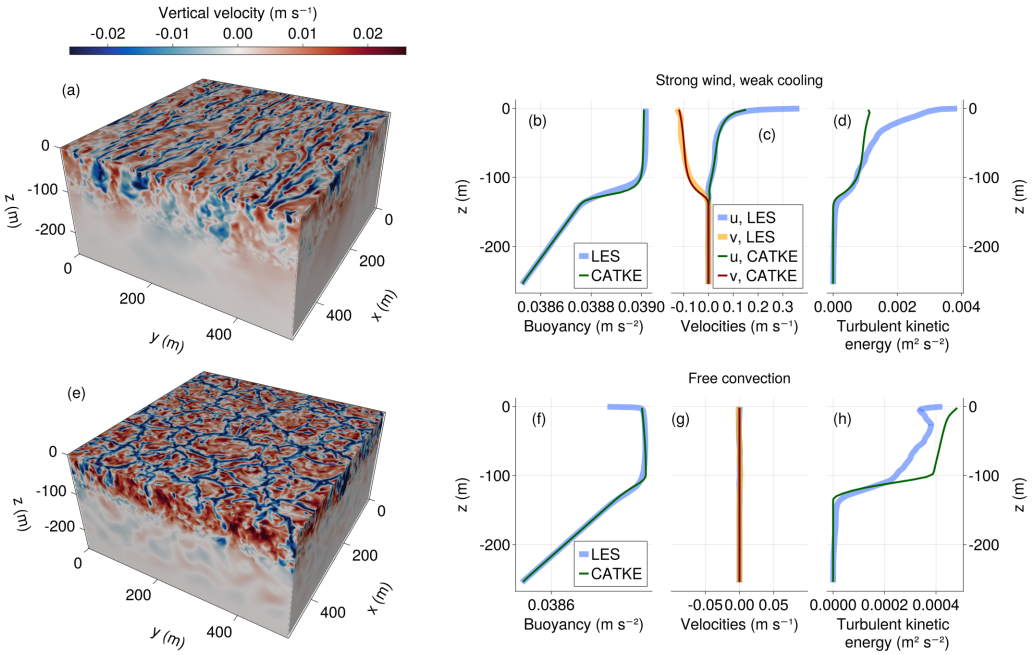

Figure 1. Visualization of large eddy simulations (LES) and single column simulations of the ocean surface boundary layer for (top) "strong wind, weak cooling" and (bottom) "free convection". The left panel visualizes LES vertical velocity and the right three panels compare horizontally-averaged buoyancy, horizontal velocities, and turbulent kinetic energy in LES and as predicted by CATKE.

2 CATKE formulation in a single column context

We describe CATKE in a one-dimensional single column context. Single column models describe the horizontally-averaged dynamics of a horizontally-periodic large eddy simulation like that depicted in figure 1, and idealizes the evolution of momentum and tracers in a horizontally-homogeneous patch of ocean. For this we first define an average $\overline{()}$ over horizontal scales 100 meters and larger, as appropriate. For example, in the context of horizontally-periodic LES the horizontal average is taken over the entire domain. We then decompose all three-dimensional variables Ψ into a horizontally-averaged component $\psi \overset{\text{def}}{=} \bar{\Psi}$

and a fluctuation ψ' such that,

$$\Psi(x,y,z,t) = \underbrace{\bar{\Psi}(z,t)}_{\stackrel{\text{def}}{=}\psi(z,t)} + \psi'(x,y,z,t)\,, \tag{1}$$

where $\Psi \in (U,V,W,C)$ includes the velocity components U,V,W and tracer concentrations C. We assume the ocean is horizontally-homogeneous, or nearly so, such that $W \approx w'$. The single-column, horizontally-averaged zonal momentum $u(z,t)$, meridional momentum $v(z,t)$, and any tracer $c(z,t)$ obey

$$\partial_t u - fv = -\partial_z \overline{w'u'}\,, \tag{2}$$
$$\partial_t v + fu = -\partial_z \overline{w'v'}\,, \tag{3}$$
$$\partial_t c = -\partial_z \overline{w'c'}\,, \tag{4}$$

where f is the Coriolis parameter. Lateral fluxes vanish from (2)–(4) due to horizontal homogeneity.

CATKE models the horizontally-averaged vertical fluxes $\overline{w'\psi'}$ appearing on the right side of (2)–(4) with a mixing length formulation (Prandtl et al., 1925),

$$\overline{w'\psi'} \approx -\underbrace{\ell_\psi \sqrt{e}}_{\stackrel{\text{def}}{=}\kappa_\psi}\, \partial_z \psi\,, \tag{5}$$

where e is the turbulent kinetic energy, $\sqrt{e}$ is the turbulent velocity scale, and ℓ_ψ is the mixing length for the horizontally-averaged variable $\psi(z,t)$. After choosing to parameterize turbulent transport with eddy diffusion that depends on the turbulent velocity $\sqrt{e}$ and mixing length ℓ_ψ, the form $\kappa_\psi = \ell_\psi \sqrt{e}$ follows from dimensional analysis. CATKE invokes three mixing lengths and three eddy diffusivities: one for horizontal velocities, ℓ_u, one for tracers, ℓ_c, and one for turbulent kinetic energy, ℓ_e. With (5), the single column equations become

$$\partial_t u - fv = \partial_z \left(\kappa_u \partial_z u\right)\,, \tag{6}$$
$$\partial_t v + fu = \partial_z \left(\kappa_u \partial_z v\right)\,, \tag{7}$$
$$\partial_t c = \partial_z \left(\kappa_c \partial_z c\right)\,. \tag{8}$$

In this paper we use a linear equation of state that relating density to a single thermodynamic constituent, such that the buoyancy b is just another tracer,

$$\partial_t b = \partial_z \left(\kappa_c \partial_z b\right)\,. \tag{9}$$

The buoyancy gradient $N^2 \stackrel{\text{def}}{=} \partial_z b$ appears in many of the scaling arguments central to CATKE's formulation. Note that in more realistic simulations of seawater, b and N^2 are functions of geopotential height, mean temperature, and mean salinity through the empirically-determined seawater equation of state (McDougall & Barker, 2011).

To estimate the turbulent kinetic energy e in (5), we consider an *analogy* — but not a precise relationship — between e and the kinetic energy of the subgrid velocity field, $\mathcal{E}$,

$$\mathcal{E} \stackrel{\text{def}}{=} \tfrac{1}{2}\overline{|\boldsymbol{u}'|^2} = \tfrac{1}{2}\left(\overline{u'^2} + \overline{v'^2} + \overline{w'^2}\right)\,. \tag{10}$$

The "true" subgrid kinetic energy $\mathcal{E}$ obeys

$$\partial_t \mathcal{E} = \underbrace{-\partial_z\left(\overline{w'\mathcal{E}'} + \overline{w'p'} - \nu\partial_z \mathcal{E}\right)}_{\text{transport}} \underbrace{-\,\overline{\boldsymbol{u}'w'}\cdot\partial_z \boldsymbol{u}}_{\text{shear production}} + \underbrace{\overline{w'b'}}_{\text{buoyancy flux}} \underbrace{-\,\nu\overline{|\nabla \boldsymbol{u}'|^2}}_{\text{dissipation}}\,, \tag{11}$$

where ν is the kinematic viscosity, p is kinematic pressure (dynamic pressure divided by a reference density) and $\mathcal{E}' = \frac{1}{2}|\boldsymbol{u}'|^2 - \mathcal{E}$. Inspired by (11), we formulate an equation for e consisting of terms that mirror each term in equation (11):

$$\partial_t e = \underbrace{\partial_z \left(\kappa_e \partial_z e\right)}_{\text{transport}} + \underbrace{\kappa_u |\partial_z \boldsymbol{u}|^2}_{\text{shear production}} - \underbrace{\kappa_c N^2}_{\text{buoyancy flux}} - \underbrace{\frac{e^{3/2}}{\ell_D}}_{\text{dissipation}} , \tag{12}$$

where $|\partial_z \boldsymbol{u}|^2 = (\partial_z u)^2 + (\partial_z v)^2$ is the vertical shear squared, κ_e is the vertical diffusivity of e, ℓ_D is the "dissipation length scale", and we have labeled the corresponding terms in (11) and (12). The shear production and buoyancy flux terms are formulated by applying the eddy diffusivity hypothesis (5) to their corresponding expressions in equation (11). We assume that e transport, which helps to deepen boundary layers by modeling turbulence spreading away from turbulence-generating regions, can be modeled with an eddy diffusivity $\kappa_e = \ell_e \sqrt{e}$. This transport closure is not quite right for $\mathcal{E}$ — which experiences non-local transport not least due to pressure effects in (11) — and must be interpreted in light of the approximate relationship between e and $\mathcal{E}$. Finally, to model the dissipation of e we introduce the dissipation length scale ℓ_D, which has a similar form to the mixing lengths ℓ_u, ℓ_c, and ℓ_e. The expression $e^{3/2}/\ell_D$ follows on dimensional grounds.

The *approximate* correspondence between e and $\mathcal{E}$ is important: e is a *latent variable* whose purpose is to help predict u, v, c, and other mean quantities, rather than to predict $\mathcal{E}$. Interpreting e as a latent variable rather than as the actual subgrid kinetic energy $\mathcal{E}$ is also proposed by Kolmogorov (see Spalding, 1991) and Saffman (1970) — who go so far as to model TKE production with $e|\partial_z \boldsymbol{u}|$ rather than the more closely analogous $\kappa_u |\partial_z \boldsymbol{u}|^2 \sim \ell \sqrt{e} |\partial_z \boldsymbol{u}|^2$. (As discussed in section 4.4, we model shear production with $\kappa_u |\partial_z \boldsymbol{u}|^2$ in part to lend CATKE an easily-interpretable critical Richardson number.) Physically e may be interpreted as the *part* of TKE associated with irreversible mixing, thus implicitly filtering reversible motions that contribute to $\mathcal{E}$ but not to mixing, such as internal waves generated by convective plumes that plunge through the mixed layer and penetrate the stably stratified region below. Though e is latent and unobservable, LES observations of u, v, c nevertheless well-inform its evolution because u, v, c and e are tightly coupled via (5).

Equation (12) requires boundary conditions. On all boundaries except the surface where $z = 0$, we impose no-flux conditions on e. At $z = 0$, we parameterize subgrid production of e by wind stress and destabilizing buoyancy fluxes across the uppermost cell interface with

$$Q_e\,|_{z=0} = -\mathbb{C}_Q^{\text{shear}}\, u_\star^3 - \mathbb{C}_Q^{\text{conv}}\, \max(Q_b, 0) \Delta z \,, \tag{13}$$

where $\mathbb{C}_Q^{\text{shear}}$ and $\mathbb{C}_Q^{\text{conv}}$ are constant, non-dimensional free parameters, Q_b is the surface buoyancy flux defined such that $Q_b > 0$ removes buoyancy and thus causes convection, Δz is the distance between the top of the ocean domain and the first interior cell interface, and $u_\star$ is the friction velocity,

$$u_\star \overset{\text{def}}{=} \left(Q_u^2 + Q_v^2\right)^{1/4} , \tag{14}$$

defined in terms of the zonal and meridional kinematic momentum fluxes Q_u and Q_v (wind stresses divided by reference water density). Note that other one equation parameterizations only use $u_\star$ in their surface boundary condition for e (Blanke & Delecluse, 1993; Madec et al., 2017).

The surface flux parameterization (13) introduces the notation

$$\mathbb{C}_{\text{component}}^{\text{label}} \tag{15}$$

for two free parameters $\mathbb{C}_Q^{\text{shear}}$ and $\mathbb{C}_Q^{\text{conv}}$, where "label" indicates the parameter's role and "component" refers to the variable or component to which the parameter associates.

2.1 Turbulence length scale model

We decompose the four length scales $\ell_\psi \in (\ell_u, \ell_c, \ell_e, \ell_D)$ into a convective length scale ℓ_ψ^{conv} and a "shear" length scale ℓ_ψ^{shear}. At any time and location, the maximum of these two length scales is chosen as the mixing length via

$$\ell_\psi = \max\left(\ell_\psi^{\text{conv}}, \ell_\psi^{\text{shear}}\right) , \tag{16}$$

encapsulating a sharp separation between turbulence regimes that exhibit distinct scaling laws. (Despite its name, the "shear" length scale ℓ^{shear} is active in non-convective turbulence mixing without shear, as explored in section 4.2.) We next describe a length scale formulation that can be calibrated to predict turbulent fluxes associated with the kinds of flows plotted in figure 1.

2.1.1 Shear turbulence length scale

To represent non-convective turbulence either in strong stratification or near the ocean surface, we use the length scale

$$\ell_\psi^{\text{shear}} = \sigma_\psi(Ri) \min\left(\frac{\sqrt{e}}{N_+}, \mathbb{C}^s d\right) , \quad \text{where} \quad N_+^2 \stackrel{\text{def}}{=} \max\left(0, \partial_z b\right) \tag{17}$$

where d is the distance to the ocean surface, $\mathbb{C}^s$ is a free parameter ("s" for "surface"), and σ_ψ is a "stability function" defined below. $\sqrt{e}/N$ is the vertical distance traversed by a patch of turbulence expending all its kinetic energy e to mix the uniform stratification N. $\sqrt{e}/N$ is a local or constant stratification version of the more complete, but computationally expensive length scale proposed by Gaspar et al. (1990).

We use (17) for ℓ_c^{shear}, ℓ_u^{shear}, and ℓ_e^{shear}. For the dissipation length scale ℓ_D^{shear}, we use

$$\ell_D = \frac{1}{\sigma_D(Ri)} \min\left(\frac{\sqrt{e}}{N_+}, \mathbb{C}^s d\right) . \tag{18}$$

The alternative stability function formulation in (18) yields a tight connection between σ_D's free parameters and e dissipation, and facilitates analytical calculations such as those presented in section 4.

The stability functions σ_ψ in (17)–(18) modulate each length scale with the stably-stratified Richardson number

$$Ri \stackrel{\text{def}}{=} \frac{N_+^2}{|\partial_z \boldsymbol{u}|^2} , \tag{19}$$

which, among other meanings, measures the role of shear production in the dynamics of turbulent mixing. The stability functions give CATKE a variable turbulent Prandtl number,

$$Pr = \frac{\kappa_u}{\kappa_c} , \tag{20}$$

which has a well-established relationship with Ri in atmospheric boundary layers (D. Li, 2019).

We use piecewise linear functions for $\sigma_\psi(Ri)$,

$$\sigma_\psi(Ri) = \mathbb{C}_\psi^{\text{lo}} + \left(\mathbb{C}_\psi^{\text{hi}} - \mathbb{C}_\psi^{\text{lo}}\right) \text{ clamp}\left(\frac{Ri - \mathbb{C}_{Ri}^0}{\mathbb{C}_{Ri}^\delta}\right) , \quad \text{where} \quad Ri \stackrel{\text{def}}{=} \frac{N_+^2}{|\partial_z \boldsymbol{u}|^2} , \tag{21}$$

and $\text{clamp}(x) = \max\left[0, \min(1, x)\right]$. The parameter $\mathbb{C}_{Ri}^0$ is the "transition Ri". For low $Ri < \mathbb{C}_{Ri}^0$, the stability function is constant with $\sigma_\psi = \mathbb{C}_\psi^{\text{lo}}$. For larger $Ri > \mathbb{C}_{Ri}^0$, σ_ψ transitions linearly in Ri to $\mathbb{C}_\psi^{\text{hi}}$ over a range $\mathbb{C}_{Ri}^\delta$. For high $Ri > \mathbb{C}_{Ri}^0 + \mathbb{C}_{Ri}^\delta$, the stability function is again constant with $\sigma_\psi = \mathbb{C}_\psi^{\text{hi}}$.

The four shear length scales introduce 11 free parameters: $\mathbb{C}^s$, $\mathbb{C}^\delta_{Ri}$, and $\mathbb{C}^0_{Ri}$ used in all four length scales, along with 8 additional parameters associated with the two limiting coefficients $\mathbb{C}^{\text{lo}}_\psi$ and $\mathbb{C}^{\text{hi}}_\psi$ for each length scale respectively. Note that because κ_u and κ_c each scale with σ_u and σ_c, our Pr is a continuous rational function of Ri, unlike, for example, the piecewise constant Pr proposed by Blanke and Delecluse (1993). The turbulent Prandtl number for shear turbulence becomes,

$$Pr = \frac{\kappa_u}{\kappa_c} = \frac{\sigma_u}{\sigma_c}\,, \qquad \text{such that} \qquad \underbrace{\frac{\mathbb{C}^{\text{lo}}_u}{\mathbb{C}^{\text{lo}}_c}}_{Ri\,<\,\mathbb{C}^0_\sigma} \;\le\; Pr \;\le\; \underbrace{\frac{\mathbb{C}^{\text{hi}}_u}{\mathbb{C}^{\text{hi}}_c}}_{Ri\,\ge\,\mathbb{C}^0_\sigma+\mathbb{C}^\delta_\sigma} \,. \tag{22}$$

The limiting Pr values $\mathbb{C}^{\text{lo}}_u/\mathbb{C}^{\text{lo}}_c \approx 0.9$ and $\mathbb{C}^{\text{hi}}_u/\mathbb{C}^{\text{hi}}_c \approx 1.7$ are determined by calibration, as described in section 3.

2.1.2 Convective turbulence length scale

To formulate a model for the convective length scale, we divide the convective boundary layer into two regions: a "convecting layer" with unstable $N^2 < 0$, and a "penetration layer" with thickness δ. The penetration layer then includes heights z where $N^2(z) > 0$ but $N^2(z+\delta) < 0$. (We use "penetration layer" rather than "entrainment layer" used by Deardorff et al. (1970) because it is less likely to be confused with other types of "entrainment".) Our formulation for the convective length scale models both rapid mixing in the convective layer as well as entrainment into the boundary layer from below by plumes plunging through the convecting layer into the stably stratified penetration layer below. We use a convective length scale for tracers, TKE, and TKE dissipation, but not for momentum.

Our dynamic length scale for mixing in the convective layer is based on a dimensional analysis first proposed by Deardorff et al. (1970) that links the turbulent velocity $\sqrt{e}$ ($\mathrm{m\,s^{-1}}$), surface buoyancy flux Q_b ($\mathrm{m^2/s^3}$), and convective layer depth, h (m),

$$\sqrt{e} \sim (h\,Q_b)^{1/3}\,. \tag{23}$$

Recasting (23) in terms of a time-scale $t_{\text{mix}} \sim h/\sqrt{e}$ for mixing over the convective depth h yields

$$t_{\text{mix}} \sim \left(\frac{h^2}{Q_b}\right)^{1/3} \sim \frac{h^2}{\kappa_c}\,. \tag{24}$$

The second relationship in (24) expresses t_{mix} in terms of the tracer diffusivity κ_c. Consider convection driven by constant destabilizing buoyancy fluxes Q_b and increasing $h(t)$: the mixing time then evolves according to $t_{\text{mix}} \sim h^{2/3}$. On the other hand, with *constant* κ_c — a commonly used parameterization when $N^2 < 0$ (Madec et al., 2017; Kuhlbrodt et al., 2018; Gutjahr et al., 2021; Jungclaus et al., 2022) — we find that $t_{\text{mix}} \sim h^2$. Thus constant convective adjustment diffusivities inaccurately exhibit $t_{\text{mix}} \sim h^2$ and may produce bias when convection competes with other processes such as lateral restratification, or biogeochemical production and destruction.

To capture t_{mix} in (24) for the convective region where $N^2 < 0$, we introduce a dynamic convective mixing length scale ℓ^h_ψ that scales with h,

$$\ell^h_\psi \overset{\text{def}}{=} \mathbb{C}^h_\psi \frac{e^{3/2}}{\widetilde{Q}_b + Q^{\min}_b} \sim h\,, \tag{25}$$

where the regularizer $Q^{\min}_b$ is a minimum convective buoyancy flux parameter chosen small enough to have no impact on CATKE-parameterized solutions, and $\widetilde{Q}_b$ is an estimate of the slowly-evolving part of the buoyancy flux Q_b averaged over time-scales $t \sim t_{\text{mix}}$. We

compute $\widetilde{Q}_b$ by integrating

$$\partial_t \widetilde{Q}_b = \underbrace{\left(\frac{Q_b}{\ell_D^2(z=0)}\right)^{1/3}}_{\sim t_{\rm mix}^{-1}} \left(Q_b - \widetilde{Q}_b\right) , \tag{26}$$

where ℓ_D is the dissipation length scale and $(\ell_D^2/Q_b)^{1/3} \sim t_{\rm mix}$ scales with the instantaneous convective mixing time. Note that in quasi-equilibrium $\widetilde{Q}_b \approx Q_b$. Because $\ell_\psi^h \sim h$, CATKE's convective tracer diffusivity scales with $\kappa_c \sim h\sqrt{e}$.

The second objective of our convective mixing length formulation is to correctly predict $h(t)$. For this we introduce a model for "penetrative mixing" *below* the convective mixed layer associated with convective plumes that plunge through the mixed layer and penetrate into the strongly stratified region below. The "empirical law of convection" (Large et al., 1994; Siebesma et al., 2007; Van Roekel et al., 2018; Souza et al., 2020, 2022) is the observation, robust across a wide range of convective conditions, that penetrative fluxes at the penetration level z_p scale with

$$\overline{w'b'}\,|_{z=z_p} \sim -Q_b \qquad \text{such that} \qquad h^2 \sim \frac{Q_b t}{N^2} , \tag{27}$$

for initially constant buoyancy gradient N^2 and constant Q_b.

To ensure that CATKE reproduces (27), we introduce a "penetrative mixing length",

$$\ell_\psi^p \overset{\rm def}{=} \mathbb{C}_c^p \frac{\widetilde{Q}_b}{N^2\sqrt{e} + Q_b^{\rm min}} , \tag{28}$$

which is applied at the height $z_p < 0$ defined via

$$N^2(z_p) > 0 \qquad \text{and} \qquad N^2(z_p + \delta) < 0 , \tag{29}$$

where δ is the thickness of the penetration layer. At $z = z_p$, (28) produces $\overline{w'b'} = -\ell_c^p N^2 \approx -\widetilde{Q}_b$ in accordance with the empircal law in (27). Our current numerical implementation of the convective mixing length uses $\delta = \Delta z$ where Δz is the grid spacing at z_p. This choice amounts to an assumption that δ is thinner than the grid spacing Δz.

Finally, we note that because e is much larger in shear turbulence than in convective turbulence with similar mixing rates (for example, compare figure 1(d) and (h)), the scaling (25) will greatly overestimate the mixing length when e is produced by both convection and shear. To limit the impact of the convective mixing length in the presence of shear, we use the non-dimensional "sheared plume number",

$$Sp(z) \overset{\rm def}{=} \frac{|\partial_z \boldsymbol{u}| e}{\widetilde{Q}_b + Q_b^{\rm min}} , \tag{30}$$

and reduce the convective mixing length by

$$\max\left(0, 1 - \mathbb{C}^{sp}\, Sp\right) , \tag{31}$$

where $\mathbb{C}^{sp}$ is a free parameter. The reduction factor (31) is used in lieu of more detailed understanding of how shear acts to limit turbulence correlation scales during convection. We anticipate that (30) increases as shear production of TKE increases relative to buoyancy flux during convection.

Putting (25), (28), and (31) together yields the piecewise parameterization

$$\ell_\psi^{\rm conv}(z) = \max\left(0, 1 - \mathbb{C}^{sp}\, Sp\right) \begin{cases} \ell_\psi^h & \text{if } N^2 < 0 \text{ and } Q_b > 0 , \\ \ell_\psi^p & \text{if } N^2 > 0 , N^2(z + \Delta z) < 0 , \text{ and } Q_b > 0 , \\ 0 & \text{otherwise} . \end{cases} \tag{32}$$

Figure 2 illustrates the behavior of the convective length scale predicted by CATKE in (32) for three free convection cases with surface buoyancy fluxes $Q_b = 9.6 \times 10^{-7}$, 2.4×10^{-7}, and $8.8 \times 10^{-8}\,\mathrm{m^2\,s^{-3}}$ integrated for 6, 24, and 72 hours respectively, using the initial buoyancy profile in equation (A1), which is also used for all our LES. Figure 2(a) shows CATKE-simulated buoyancy profiles after integrating for 6, 24, and 72 hours. Figure 2(b) shows that stronger forcing cases have greater levels of turbulent kinetic energy. Figure 2(c) shows the tracer mixing length, which above $z = -100$ meters is dominated by the convective mixing length. Though each case has different TKE and different surface buoyancy flux, they nevertheless predict similar tracer mixing lengths which are O(100) meters and thus similar to the boundary layer depth, corroborating the dimensional analysis in equation (23). Figure 2(d) shows the eddy diffusivity for the three cases — unlike a typical constant-diffusivity convective adjustment model, CATKE's "convective adjustment diffusivity" varies depending on the strength of the surface buoyancy flux. Because the predicted mixing length is similar for all three cases, the tracer diffusivity varies with the surface buoyancy flux due to variation in the turbulent kinetic energy.

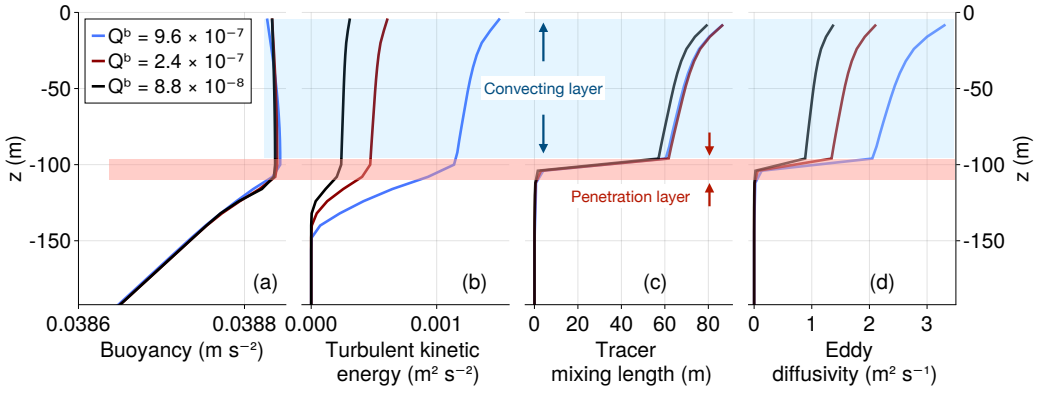

Figure 2. CATKE mixing length and eddy diffusivity during free convection for three cases with boundary layer depth $h \approx 100$ m. (a) CATKE-predicted buoyancy profiles for the three cases, (b) profiles turbulent kinetic energy, e, (c) tracer mixing lengths ℓ_c, (d) tracer eddy diffusivities κ_c. Blue shades the unstable "convecting layer" where $N^2 < 0$ and thus $\ell_c \sim h \sim e^{3/2}/Q_b$. Red shades the "penetration layer" just below the unstable convecting layer, where $N^2(z) > 0$ but $N^2(z + \Delta z) < 0$. The buoyancy fluxes Q_b in panel (a) have units $\mathrm{m^2\,s^{-3}}$.

3 Calibration and assessment in the single column context

CATKE's 18 free parameters are listed in table 3. We calibrate CATKE's 18 free parameters in an *a posteriori* (Duraisamy, 2021; Frezat et al., 2022) single-column context using horizontally-averaged data from 18 LES briefly described in section 1 and in more detail in Appendix A. Our *a posteriori* calibration method poses a Bayesian inverse problem that models the mismatch between LES data and predictions of the LES data generated by 36 independent CATKE-parameterized single column models at 4- and 8-meter vertical resolution. We use Ensemble Kalman Inversion (Iglesias et al., 2013) to find optimal parameters that minimize this model-data mismatch.

Using *a posteriori* calibration is crucial: because we use *predictions* generated by CATKE-parameterized single-column models to estimate model-data mismatch, our calibration method incorporates numerical error, prediction bias, and can leverage indirect data. For example, our calibration constrains parameters in the TKE equation despite that the

Symbol	Description	Optimal value	Bounds
$\mathbb{C}_Q^{\text{shear}}$	Wind stress TKE surface flux	1.1	$(0, 4)$
$\mathbb{C}_Q^{\text{conv}}$	Convective TKE surface flux	4.0	$(0, 8)$
$\mathbb{C}^s$	Stratification-limited mixing scale	2.4	$(0, 4)$
$\mathbb{C}_c^{\text{lo}}$	Tracer mixing for low Ri	0.2	$(0, 1)$
$\mathbb{C}_c^{\text{hi}}$	Tracer mixing for high Ri	0.045	$(0, 1)$
$\mathbb{C}_u^{\text{lo}}$	Velocity mixing for low Ri	0.19	$(0, 1)$
$\mathbb{C}_u^{\text{hi}}$	Velocity mixing for high Ri	0.086	$(0, 1)$
$\mathbb{C}_e^{\text{lo}}$	TKE transport for low Ri	1.9	$(0, 4)$
$\mathbb{C}_e^{\text{hi}}$	TKE transport for high Ri	0.57	$(0, 4)$
$\mathbb{C}_D^{\text{lo}}$	Dissipation scale for low Ri	1.1	$(0, 4)$
$\mathbb{C}_D^{\text{hi}}$	Dissipation scale for high Ri	0.37	$(0, 4)$
$\mathbb{C}_{Ri}^{\delta}$	Stability function Ri width	0.45	$(0, 1)$
$\mathbb{C}_{Ri}^{0}$	Stability function transitional Ri	0.47	$(0, 1)$
$\mathbb{C}_c^h$	Tracer free convection scale	1.5	$(0, 2)$
$\mathbb{C}_c^p$	Tracer free entrainment scale	0.2	$(0, 1)$
$\mathbb{C}_D^h$	Dissipation free convection scale	0.88	$(0, 2)$
$\mathbb{C}_e^h$	TKE free convection scale	1.2	$(0, 2)$
$\mathbb{C}^{sp}$	Sheared plume scale	0.14	$(0, 2)$

Table 1. A summary of CATKE's free parameters. Note that "low Ri" means $Ri \le \mathbb{C}_{Ri}^0$, while "high Ri" means $Ri \ge \mathbb{C}_{Ri}^0 + \mathbb{C}_{Ri}^\delta$.

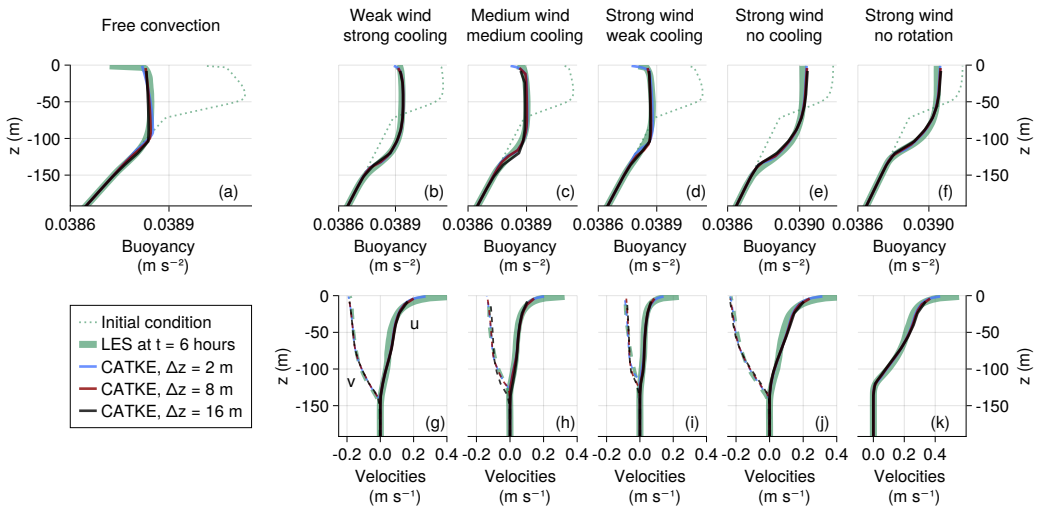

Figure 3. Comparison between CATKE and six strongly-forced large eddy simulations run for 6 hours.

calibration to LES data includes only buoyancy and velocity profiles — because TKE is tightly coupled to the evolution of tracers and momentum through (5). Our calibration also accounts for our particular implementation of CATKE on a staggered vertical grid and incorporates spatial- and time-discretization error.

3.1 Pointwise error for 6- and 72-hour suites

We validate CATKE with optimal parameters against 12 additional LES: 6 more strongly-forced and 6 more weakly-forced than the LES used for calibration. All LES used for both calibration and assessment use the same initial buoyancy profile. In the strongly-forced cases, the boundary layer deepens to ∼100 meters in 6 hours. (The strongest buoyancy flux is comparable to $2000\,\mathrm{W\,m^{-2}}$ and the strongest wind stress is comparable to atmospheric winds of $25\,\mathrm{m\,s^{-1}}$.) Figure 3 shows the LES profiles and CATKE predictions generated with 2-, 4-, and 8-meter vertical resolution. In general the predictions of the CATKE-parameterized single column model are accurate and resolution-independent. In free convection, the CATKE-predicted buoyancy exhibits a more unstable buoyancy profile than LES in the upper part of the boundary layer. We link this bias to CATKE's eddy diffusivity formulation (5): free convection exhibits upgradient buoyancy fluxes which cannot be described by a downgradient eddy diffusivity model. Yet because buoyancy is almost perfectly mixed in the upper part of the boundary layer, the impact of this buoyancy gradient bias is minor.

We next assess CATKE for weakly-forced cases in which the boundary layer deepens by 100 meters over 72 hours. Figure 4 assess CATKE against LES with weaker forcing than used for calibration. The challenging weakly-forced "strong wind no cooling" case is the one case where CATKE-parameterized solutions exhibit discernible resolution dependence.

4 Exhibition of CATKE dynamics

In this section, we simulate several turbulence scenarios pertinent to oceanic microturbulent mixing to explore CATKE's dynamics and to nurture future calibration efforts. We consider diurnal forcing, stratified mixing by a turbulent source in quiescent mean flow, and forced stratified shear mixing.

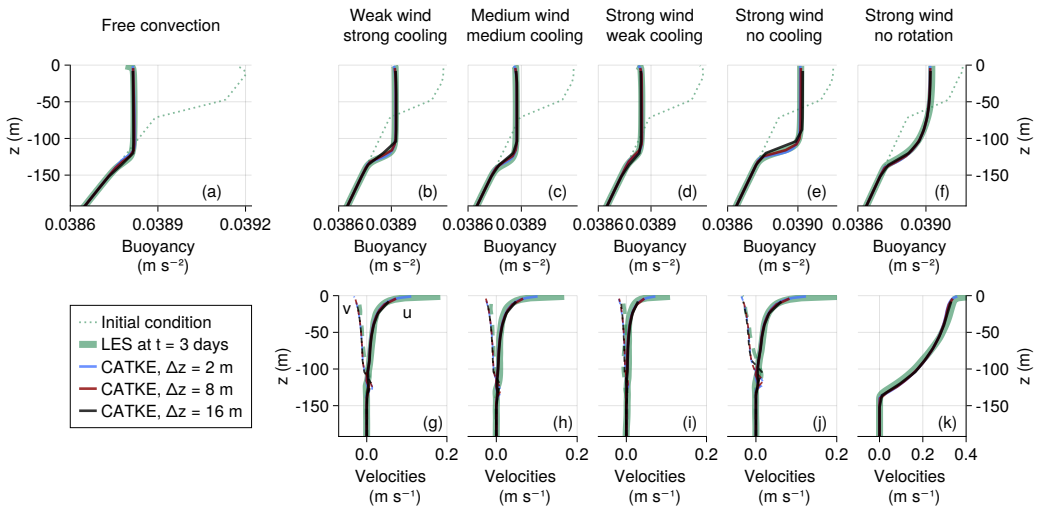

Figure 4. Comparison between CATKE and six weakly-forced large eddy simulations run for 72 hours.

4.1 Diurnal boundary layer

To investigate CATKE's response to fluctuating buoyancy fluxes, we simulate the deepening of a one-dimensional surface boundary layer beneath light winds and "diurnal" buoyancy fluxes that oscillate from heating to cooling. Diurnal variations in boundary layer turbulence and heat content driven by diurnal variations in incoming and outcoming radiations are widespread in the summertime and tropical ocean (Price et al., 1986; Moulin et al., 2018; Hughes et al., 2020). We choose a scenario with constant momentum flux $Q_u = -4 \times 10^{-5}\,\mathrm{m^2\,s^{-2}}$ and the fluctuating buoyancy flux

$$Q_b(t) = Q_n - Q_s \max\left[0, \sin\left(\tfrac{2\pi}{1\,\mathrm{day}} t + \pi\right)\right] , \tag{33}$$

with outgoing (cooling) buoyancy flux $Q_n = 10^{-7}\mathrm{m^2\,s^{-3}}$ and incoming (heating) buoyancy flux $Q_s = 4 \times 10^{-7}\,\mathrm{m^2\,s^{-3}}$, corresponding to a boundary layer driven by light winds, diurnally-varying incoming solar radiation, and constant outgoing solar radiation (see for example figure 5 in Moulin et al. (2018) and figure 6 in Sarkar and Pham (2019)). Note that with our flux convection, $Q_b > 0$ is destabilizing and corresponds to buoyancy loss from the surface, while $Q_b < 0$ corresponds to heating. Similarly, a negative x-momentum flux $Q_u < 0$ drives flow in the $+x$-direction. The diurnal cycle in (33) is shifted so that the sun rises at $t = 0$. A time-series of the buoyancy flux is shown in figure 5(a).

We initialize with uniform stratification $N^2 = 10^{-5}\,\mathrm{s^{-2}}$ and run the simulation for 4.5 days. Figure 5(c), (e), (g), and (i) show depth-time diagrams of the resulting buoyancy b, turbulent kinetic energy e, tracer diffusivity κ_c, and tracer mixing length ℓ_c. Figure 5(j) shows $L_c(t) = \max \ell_c(z,t)$ within the column at each time t. Vertical profiles of b, e, κ_c, and ℓ_c are shown figure 5b, (d), (f) and (h). Note the logarithmic x-axis in panel (h) and the logarithmic y-axis in panel (j). Between $t = 0$ and $t = 12$ hours, the boundary layer is heated while mixed by the wind, producing a strong, stable stratification close to the surface. From $t = 12$ hours to $t = 24$ hours, the surface buoyancy flux switches to destabilizing and strong mixing ensues, leading to increasing TKE e, tracer diffusivity κ_c, and tracer mixing length ℓ_c. Like observations of similar scenarios reported by Moulin et al. (2018), turbulence dissipates soon after warming begins begins except within a thin layer close to the surface, driven by shear associated with the light constant wind stress. Figures 5(e), (g), (i) show how turbulence and mixing penetrates progressively deeper over the 4 simulated

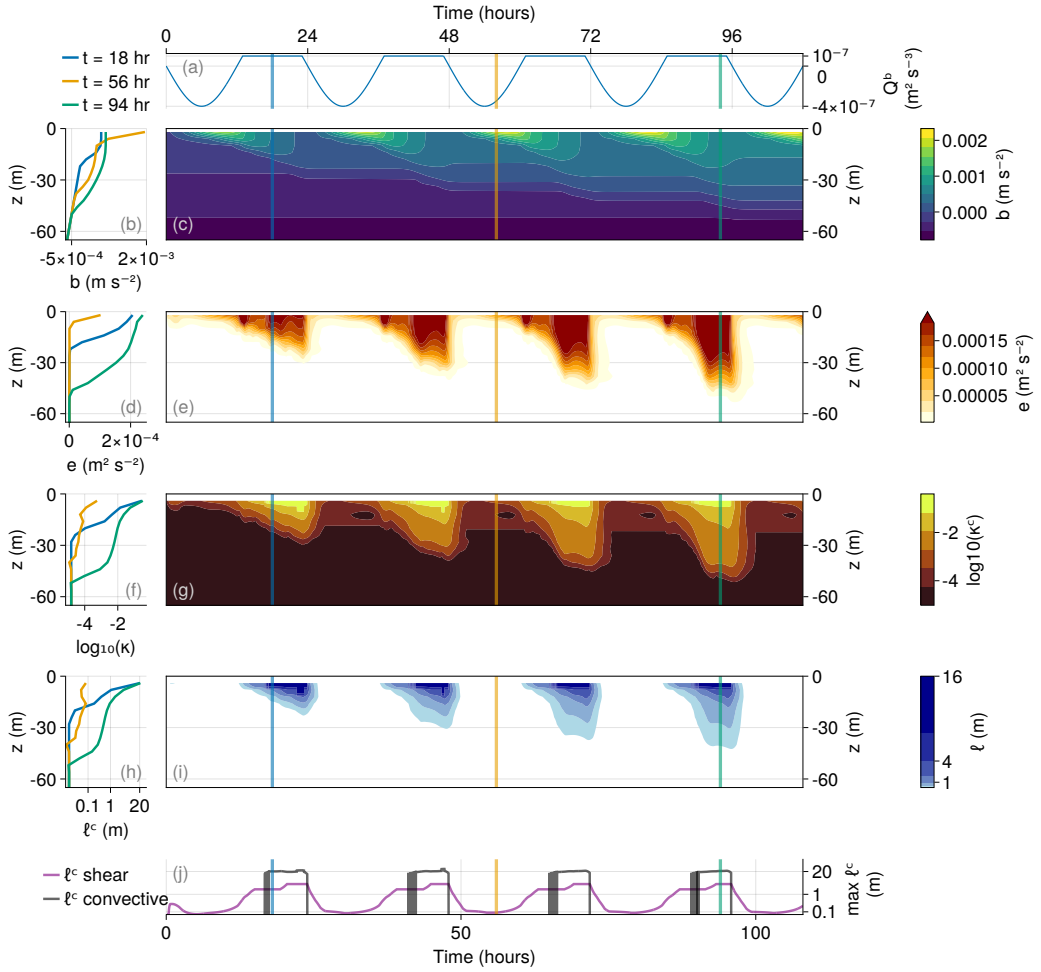

Figure 5. CATKE-parameterized simulation of a diurnal boundary layer forced by oscillatory buoyancy flux and light wind stress. The panels show (a) the surface buoyancy flux time-series, (b) profiles of buoyancy b at $t = 18, 56$, and 94 hours, (c) a depth-time diagram of buoyancy b, (d) profiles of TKE e, (e) a depth-time diagram of e, (f) profiles of the logarithm of tracer diffusivity, $\log_{10} \kappa_c$, (g) a depth-time diagram of $\log_{10} \kappa_c$, (h) profiles of the tracer mixing length ℓ_c, (i) a depth-time diagram of ℓ_c, and (j) a time-series of the maximum shear and convective tracer mixing lengths. Note the logarithmic x-axis in panel (h) and the logarithmic y-axis in panel (j).

cycles, though the column maximum mixing length plotted in figure 5 is roughly constant. We take the qualitative plausibility of these results compared to similar LES results reported by (Sarkar & Pham, 2019) (which differ in some details, such as the use of two active tracers, Coriolis force, and more) as promising that CATKE, if calibrated properly is capable of predicting boundary layer evolution beneath diurnally varying fluxes. Further validation and re-calibration to data relevant to diurnal boundary layers awaits.

4.2 Mixing by turbulence produced by an external source

To illustrate that CATKE can describe mixing outside the ocean surface boundary layer, we consider a scenario in which an initially uniform buoyancy gradient is mixed by

turbulence produced by a transient external source P, The external source is

$$P(z,t) = P_0 \exp\left\{-\frac{z^2}{2h^2} - \frac{(t-\tau)^2}{2\tau^2}\right\}, \tag{34}$$

In (34), P_0 is the characteristic power of the external source, h is the vertical extent of the source and τ is the lifetime of the transient source. This scenario is relevant to mixing by breaking internal waves, for example, generated by internal tides during a peak in the tidal cycle. In this relatively simple scenario far from boundaries and absent shear, all length scales reduce to

$$\ell_\psi \sim \frac{\sqrt{e}}{N}, \qquad \text{such that} \qquad \kappa_\psi = \ell_\psi \sqrt{e} \sim \frac{e}{N}. \tag{35}$$

Adding the external source (34) and simplifying with (35), the buoyancy and TKE equations (8) and (12) become

$$\partial_t b = \partial_z \left(\mathbb{C}_c^{\text{hi}}\, e\, N\right), \tag{36}$$

$$\partial_t e - \partial_z \left(\mathbb{C}_e^{\text{hi}} \frac{e}{N} \partial_z e\right) = P - \left(\mathbb{C}_c^{\text{hi}} + \mathbb{C}_D^{\text{hi}}\right) e\, N. \tag{37}$$

The buoyancy flux is $-\mathbb{C}_c^{\text{hi}} e\, N$ and the dissipation rate is $\mathbb{C}_D^{\text{hi}} e\, N$.

Figure 6 shows a simulation of (36)–(37) for initial condition $e = 10^{-6}\,\text{m}^2\,\text{s}^{-2}$, $P_0 = 10^{-6}\,\text{m}^2\,\text{s}^{-2}/(1\,\text{hour}) = 2.7 \times 10^{-6}\,\text{m}^2\,\text{s}^{-3}$, $h = 16$ meters, $\tau = 6$ hours, and $b = N_0^2 z$ with $N_0^2 = 10^{-6}\,\text{s}^{-2}$. Figure 6(a) and (b) show profiles and depth-time diagrams of the buoyancy gradient $N^2(z,t)$, which is diminished in the center of the domain at late times and exhibits sharp maxima on the turbulent/non-turbulent interface at the upper and lower edge of the mixing region. Figure 6(c) plots the turbulent production P, buoyancy flux, and dissipation at $t = 6$ hours. Figure 6(d) and (e) shows profiles and depth-time diagrams of the turbulent kinetic energy $e(z,t)$.

Figure 6(c) plots profiles of three terms appearing on the right hand side of (37),

$$\text{production} = P, \qquad \text{buoyancy flux} = -\mathbb{C}_c^{\text{hi}} e N, \quad \text{and} \quad \text{dissipation} = \mathbb{C}_D^{\text{hi}} e N. \tag{38}$$

The oft-scrutinized "mixing coefficient" (Gregg et al., 2018; Colm-cille, 2020) — the ratio between the buoyancy flux and dissipation contributions to the TKE budget — is

$$\Gamma \overset{\text{def}}{=} -\frac{\text{buoyancy flux}}{\text{dissipation}} = \frac{\mathbb{C}_c^{\text{hi}}}{\mathbb{C}_D^{\text{hi}}}, \tag{39}$$

and therefore a model constant determined by calibration. For the "optimal" parameters in table 3, $\Gamma \approx 0.12$ — more or less consistent with the notorious observational estimate by (Osborn, 1980) for mixing by breaking internal waves at high or infinite Ri, but less than the commonly used $\Gamma = 0.2$. We leave for future work to judge whether $\Gamma \approx 0.12$ is appropriate for ocean microturbulence or whether further calibration to more comprehensive LES or observational data is required to better constrain the parameter combination $\Gamma = \mathbb{C}_c^{\text{hi}}/\mathbb{C}_D^{\text{hi}}$.

4.3 Forced stratified shear turbulence

Next, we consider a forced stratified shear turbulence scenario reminiscent of cases simulated by Smith et al. (2021) and Jackson et al. (2008). Shear-driven stratified turbulent mixing generates intense downward heat fluxes during deep cycle turbulence in the tropical ocean (Smyth & Moum, 2013; Whitt et al., 2022) and plays an important role in mixing major ocean water masses within bottom-intensified overflows (Legg et al., 2009). We model forced stratified shear turbulence generated by forcing momentum and buoyancy towards the target profiles $u_\star$ and $b_\star$,

$$u_\star \overset{\text{def}}{=} \frac{N_\star \Delta}{\sqrt{Ri_\star}} \tanh\left(\frac{z}{\Delta}\right). \qquad \text{and} \qquad b_\star \overset{\text{def}}{=} N_\star^2 z, \tag{40}$$

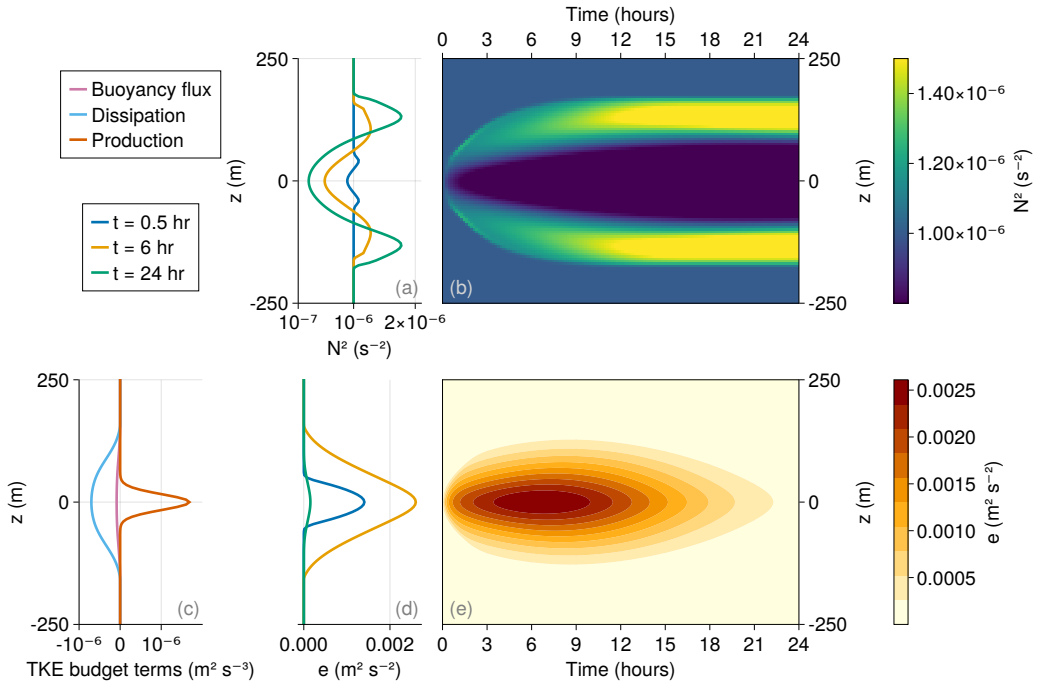

Figure 6. Simulation of mixing by turbulence produced by a transient, spatially-concentrated external source using vertical resolution $\Delta z = 5$ m and time step $\Delta t = 10$ minutes. (a) Profiles of buoyancy frequency N^2, (b) a depth-time plot of the evolution of $N^2(z,t)$, (c) the depth-dependence of terms in the TKE budget at $t = 6$ hours, (d) profiles of TKE e, (e) a depth-time plot of the evolution of $e(z,t)$.

representing a shear layer of width Δ and Richardson number $Ri_\star$ embedded in linear stratification with buoyancy frequency $N^2_\star$. We restore u and b to $u_\star$ and $b_\star$ over a time-scale τ such that

$$\partial_t b = \partial_z \left(\sigma_c \, e \, N\right) + \frac{1}{\tau} \left(b_\star - b\right) \, , \tag{41}$$

$$\partial_t u = \partial_z \left(\sigma_u \frac{e}{N} \partial_z u\right) + \frac{1}{\tau} \left(u_\star - u\right) \, , \tag{42}$$

$$\partial_t e = \partial_z \left(\sigma_e \frac{e}{N} \partial_z e\right) + \sigma_u \frac{e}{N} \left(\partial_z u\right)^2 - \left(\sigma_c + \sigma_D\right) eN \, , \tag{43}$$

where the Ri-dependent "stability functions" $\sigma_\psi(Ri)$ defined in (21) modulate CATKE's length scales via $\ell_\psi \sim \sigma_\psi \sqrt{e}/N$ and $\kappa_\psi \sim \sigma_\psi e/N$.

Figure 7 shows solutions of (41)–(43) for $Ri_\star = 0.1$, $N^2 = 10^{-6}\,\mathrm{s}^{-2}$, $d = 50$ m, $\tau = 6$ hours, with b and u initialized to $b_\star$ and $u_\star$ and initially uniform $e = 10^{-6}\,\mathrm{m}^2\,\mathrm{s}^{-2}$. The depth-time diagram of $e(z,t)$ in the middle panel of figure 7 shows an initial burst of turbulence that peaks around $t = 5$ hours. The turbulent intensity subsides between $t = 5$ hours and $t = 12$ hours, then increases subtly before leveling off around $t \approx 20$ hours.

The bottommost panel in figure 7 plots the evolution of the domain-integrated mixing coefficient Γ defined in (39), which in stably-stratified shear-driven turbulence with variable Ri takes the form

$$\Gamma(t) = \frac{\int \sigma_c e N \, \mathrm{d}z}{\int \sigma_D e N \, \mathrm{d}z} \, . \tag{44}$$

Γ exhibits a maxima at early times before settling to a steady-state value $\Gamma \approx 0.2$, which is close to the $\Gamma^{\mathrm{lo}} \approx 0.19$ that applies to uniform e and N^2 and $Ri \le \mathbb{C}^0_{Ri} \approx 0.47$. We note that Smith et al. (2021) finds Γ can reach considerably larger values than 0.2 in forced stratified shear turbulence, and that recalibration of CATKE's parameters to datasets that include forced stratified shear turbulence may be warranted.

4.4 Shear instability in CATKE

The minimum steady-state Ri plotted in figure 7(a) is $Ri \approx 0.2$. Indeed, we find that in additional experiments, the initial burst of turbulence in figure 7 disappears when $Ri_\star$ in (40) is increased beyond $Ri = 0.2$. To find the mechanism for this suppression, we follow Blanke and Delecluse (1993) and rearrange (37) for uniform e,

$$\partial_t e = \left(\sigma_c + \sigma_D\right) \, e \, N \left(\frac{Ri_c}{Ri} - 1\right) \, , \tag{45}$$

where $Ri = N^2 / \left(\partial_z u\right)^2$, and Ri_c is a "critical" Richardson number defined via

$$Ri_c \overset{\mathrm{def}}{=} \frac{\sigma_u}{\sigma_c + \sigma_D} \, . \tag{46}$$

Equation (45) means that in shear turbulence with $Ri < Ri_c$, e grows exponentially $e \sim \exp(rt)$ at the rate

$$r = \left(\sigma_c + \sigma_D\right) \, N \left(\frac{Ri_c}{Ri} - 1\right) \, . \tag{47}$$

We further elucidate the role of Ri_c by simulating forced stratified shear turbulence scenario in section 4.3 varying $Ri_\star$ between 0.05 and 0.25 while holding $\Delta = 50$ m and $N^2_\star = 10^{-6}\,\mathrm{s}^{-2}$ fixed. Figure 8 shows the integrated $E(t) = \int e \, \mathrm{d}z$, the domain-minimum $Ri_{\min}(t) = \min_z Ri(z,t)$ as a function of time, the final "equilibrium Ri" defined as $Ri_{\min}(t = 24\,\mathrm{hours})$, and the maximum $\max(E)$ for each time series.

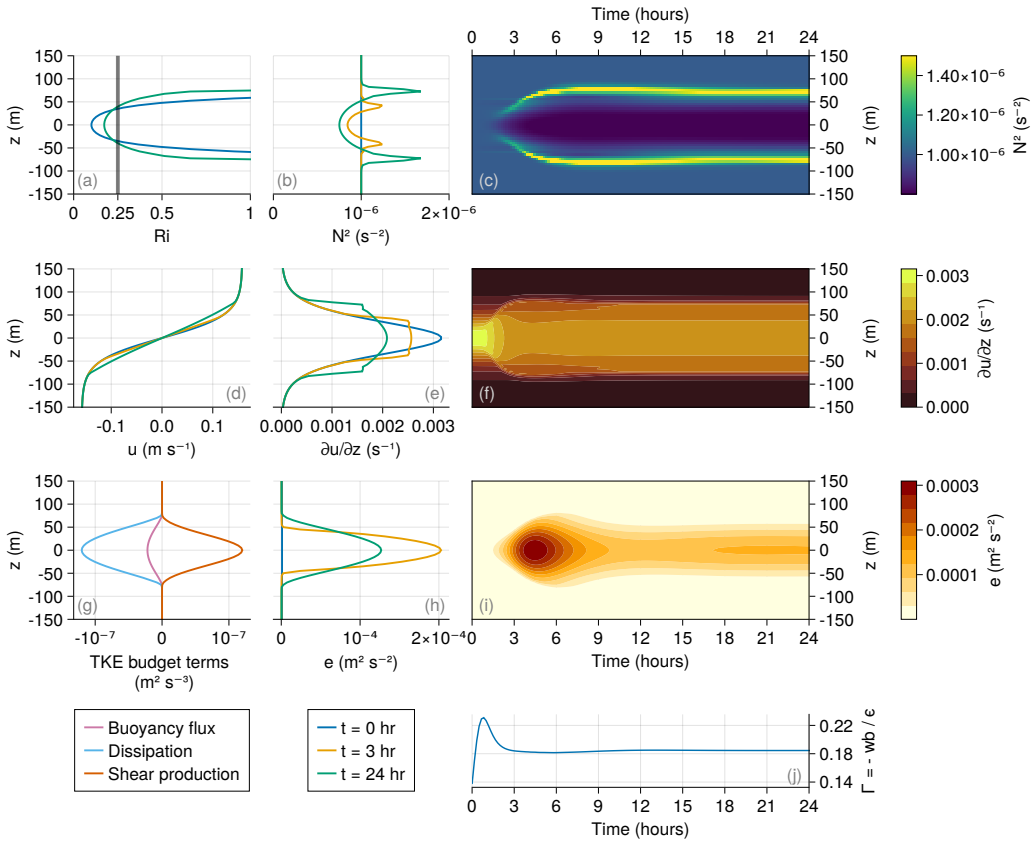

Figure 7. CATKE-parameterized simulation of mixing by forced stratified shear turbulence with vertical resolution $\Delta z = 5$ m and time step $\Delta t = 10$ minutes. Plots show the center of a domain spanning $-500\,\mathrm{m} < z < 500\,\mathrm{m}$.

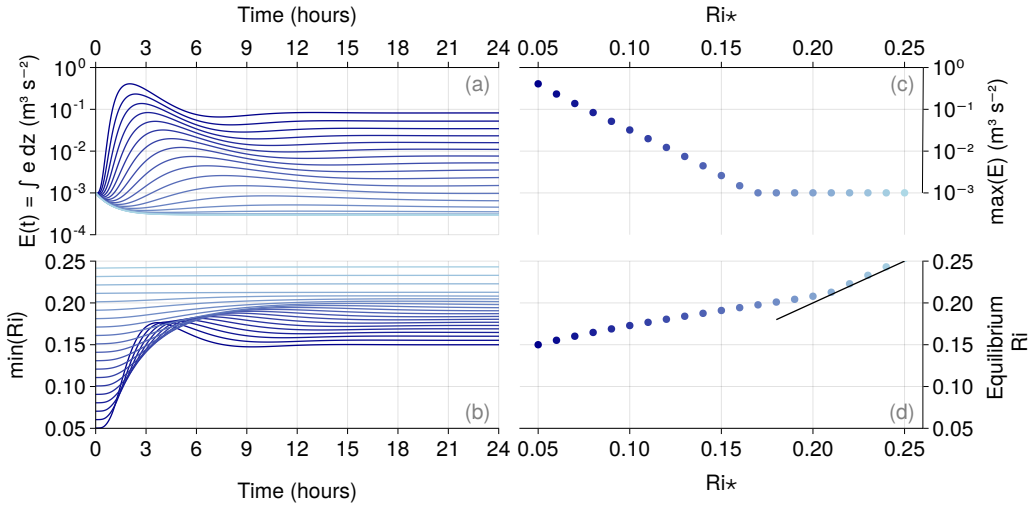

Figure 8. Transient and equilibrium characteristics of CATKE-parameterized forced stratified shear turbulence with varying target Richardson numbers $Ri_\star$. (a) evolution of vertically-integrated TKE, (b) evolution of the minimum Ri, (c) maximum vertically-integrated TKE in each simulation as a function of $Ri_\star$, (d) equilibrium or final Ri as a function of $Ri_\star$. Darker line colors in (a) and (b) correspond to smaller target $Ri_\star$.

5 Discussion

This paper describes a new one-equation parameterization for vertical fluxes by ocean microturbulence called "CATKE". CAKTE extends existing one-equation parameterizations (Blanke & Delecluse, 1993; Madec et al., 2017) with a dynamic model for convective adjustment capable of describing the wide range of convective mixing rates observed in the ocean surface boundary layer. We use *a posteriori* calibration against large eddy simulations to make a preliminary estimate of CAKTE's 18 free parameters that incorporates discretization error and treats TKE as a latent variable.

Our decision to develop a one-equation TKE-based parameterization rather than a K-profile parameterization (KPP, see Large et al., 1994; McWilliams et al., 2009; Van Roekel et al., 2018; Reichl & Hallberg, 2018; Reichl & Li, 2019) merits some discussion. KPPs have a major advantage over TKE-based parameterizations in coarse resolution ocean models (especially with different time-steps for momentum and tracer variables) because they admit time-steps as long as 2 hours (Reichl & Hallberg, 2018). In part, we are interested in one-equation parameterization here because our focus is higher resolution, mesoscale-permitting and -resolving simulations that require 1–10 minute time-steps to satisfy the advective numerical stability constraints of energetic solutions on relatively high-resolution grids. CATKE adds no additional time step constraints to such simulations, while offering some significant benefits: *(i)* dynamic prediction of diffusivity vertical structure versus prescription via "shape functions"; *(ii)* turbulent intensity growth and relaxation time scales or "memory", and *(iii)* better computational performance on hardware with fine-grained parallelism such as Graphics Processing Units (GPUs) used by Oceananigans (Ramadhan et al., 2020) and Veros (Häfner et al., 2021), which are ill-suited for the nonlinear solvers for boundary layer depth common to KPP-type models (Zhang et al., 2020).

Our calibration to a relatively limited range of LES cases reported in this paper is just the first just the first step towards using CATKE for global ocean modeling and climate projection. An important next step is to "recalibrate", or further constrain CATKE's free parameters in a global context, by minimizing the mismatch between predictions of the ocean climate state and relevant observations with global or near-global coverage. Another important piece of future work is to recalibrate CATKE to a more comprehensive suite of LES forced with temporally-varying surface fluxes, independently-varying surface waves, and horizontal flux divergences (for example following Whitt et al., 2022). More comprehensive calibration to more LES or to observations in a global context will likely reveal deficiencies to be addressed by further development of CATKE's formulation, such as accounting for the effect of surface waves on CATKE's mixing and dissipation length scales.

Appendix A A synthetic dataset generated by large eddy simulations

We use a synthetic dataset to calibrate and assess CATKE consisting of 30 idealized large eddy simulations (LES) of the ocean surface boundary layer with imposed constant surface fluxes of temperature and momentum and a simple surface wave field. The LES are initialized from rest with zero velocity and the piecewise-linear buoyancy stratification

$$b(z, t=0) = \begin{cases} N^2_{\text{surf}}\, z & \text{for } z > -48\,\text{m} \\ N^2_{\text{mid}}\, z & \text{for } -72\,\text{m} > z > -48\,\text{m} \\ N^2_{\text{deep}}\, z & \text{for } z < -72\,\text{m} \end{cases} \tag{A1}$$

with $N^2_{\text{surf}} = N^2_{\text{deep}} = 2 \times 10^{-6}\,\text{s}^{-2}$ and $N^2_{\text{mid}} = 10^{-5}\,\text{s}^{-2}$.

The 30 simulations are organized into five "suites" of six simulations each by the magnitude of their forcing. The five suites are organized by the strength of their forcing and their duration: the "6-hour suite" has the strongest forcing, and the "72-hour suite" has the weakest forcing. The five suites simulate 6, 12, 24, 48, and 72 hours of boundary layer turbulence. Each suite has six cases:

1. "free convection" with pure destabilizing buoyancy forcing,
2. "weak wind strong cooling",
3. "medium wind medium cooling",
4. "strong wind weak cooling",
5. "strong wind no cooling",
6. "strong wind no rotation" with $f = 0$.

Besides "strong wind no rotation" all cases use Coriolis parameter $f = 10^{-4}\,\mathrm{s}^{-1}$. The suites are designed to run until the boundary layer is half the total depth of the domain. We denote the surface buoyancy flux with Q_b with units $\mathrm{m}^3\,\mathrm{s}^{-2}$, and the surface kinematic momentum flux Q_u with units $\mathrm{m}^2\,\mathrm{s}^{-2}$ (i.e. wind stress divided by a reference density). The buoyancy flux is always destabilizing with $Q_b \geq 0$ (carrying buoyancy upwards, out of the boundary layer) and the momentum flux forces a current in the $+x$ direction. Cases 1–5 are ordered by decreasing Q_b and increasing $|Q_u|$. The "strong wind no rotation" case has weaker wind stress than "strong wind no cooling" because rotation hinders boundary layer deepening.

For all wind-forced cases, we additionally impose a surface wave field with a surface Stokes drift amounting to a constant "Langmuir number" $La = \sqrt{u_\star / u^{\mathrm{S}}} \approx 0.3$. Our Stokes drift prescription models a surface wave field with the friction-number-dependent peak wavenumber

$$k_p = C^k \frac{g}{u_\star^2}\,, \tag{A2}$$

where $u_\star = \sqrt{|Q_u|}$ is the water-side friction velocity, g is gravitational acceleration, and we use $C^k = 10^{-6}$.

We follow Lenain and Pizzo (2020) to estimate the depth-profiles of Stokes drift and Stokes drift shear. The Stokes drift beneath a spectrum of deep-water waves is

$$u^{\mathrm{S}}(z) = 2\int_{k_p}^{k_i} \mathrm{e}^{2kz} k\sqrt{gk}\,\chi(k)\,\mathrm{d}k\,, \tag{A3}$$

where $\chi(k)$ is a one-dimensional wave spectrum that neglects "directional spreading". The spectrum $\chi(k)$ is divided into an "equilibrium range" just above the spectral peak k_p, and a "saturation range" at even higher wavenumbers:

$$\chi(k) = \begin{cases} \frac{C_\beta}{2\sqrt{g}} a_\star k^{-5/2} & \text{for} \quad k_p < k < k_n \quad \text{(equilibrium)}\,, \\ C_B k^{-3} & \text{for} \quad k_n < k < k_i \quad \text{(saturation)}\,, \end{cases} \tag{A4}$$

where k_n is a transition wavenumber between equilibrium and saturation ranges, k_i is an upper wavenumber cutoff above which waves are assumed to be isotropic and there do not contribute to Stokes drift. $a_\star = u_\star\sqrt{\rho_w/\rho_a}$ is the air-side friction velocity defined in terms of the water-side friction velocity $u_\star$, a reference air density $\rho_a = 1.225\,\mathrm{kg\,m}^{-3}$ and water density $\rho_w = 1024\,\mathrm{kg\,m}^{-3}$. Wavenumbers *below* the spectral peak k_p are assumed too weak to contribute appreciably to Stokes drift.

Both the transition wavenumber k_n and the isotropic wavenumber k_i decrease with increasing $u_\star$:

$$k_n \overset{\mathrm{def}}{=} C_r g a_\star^{-2}\,, \tag{A5}$$

$$k_i \overset{\mathrm{def}}{=} C_i g a_\star^{-2}\,, \tag{A6}$$

where $C_r = 9.7 \times 10^{-3}$ and $C_i = 0.072$.

The Stokes drift is

$$u^{\mathrm{S}}(z) = C_\beta a_\star \int_{k_p}^{k_n} \frac{\mathrm{e}^{2kz}}{k}\,\mathrm{d}k + 2C_B\sqrt{g}\int_{k_n}^{k_i} k^{-3/2}\mathrm{e}^{2kz}\,\mathrm{d}k\,. \tag{A7}$$

Noting that $\int_{k_p}^{k_n} k^{-1} \mathrm{e}^{2kz}\,\mathrm{d}k = \mathrm{Ei}(2k_n z) - \mathrm{Ei}(2k_p z)$ where Ei is the exponential integral function, we find

$$u^{\mathrm{S}}(z) = C_\beta a_\star \left[\mathrm{Ei}(2k_n z) - \mathrm{Ei}(2k_p z)\right] + 2C_B\sqrt{g}\left[\upsilon(k_n) - \upsilon(k_i)\right] , \tag{A8}$$

and

$$\partial_z u^{\mathrm{S}} = 2C_\beta a_\star \int_{k_p}^{k_n} \mathrm{e}^{2kz}\,\mathrm{d}k + 4C_B\sqrt{g}\int_n^I \frac{\mathrm{e}^{2kz}}{\sqrt{k}}\,\mathrm{d}k\,, \tag{A9}$$

$$= C_\beta a_\star \frac{\mathrm{e}^{2k_p z} - \mathrm{e}^{2k_n z}}{|z|} + 2C_B\sqrt{\frac{2\pi g}{|z|}}\left[\mathrm{erf}\left(\sqrt{2k_n|z|}\right) - \mathrm{erf}\left(\sqrt{2k_i|z|}\right)\right] , \tag{A10}$$

for the Stokes shear.

Open Research Section

This work relied on the open source software LESbrary.jl (Wagner et al., 2023) and Oceananigans.jl (Ramadhan et al., 2020) to run LES, Oceananigans.jl to run calibration simulations, and ParameterEstimocean.jl (Wagner et al., 2022) and EnsembleKalmanProcesses.jl (Dunbar et al., 2022) for the Ensemble Kalman Inversion. Scripts for performing the calibration and running the exhibition cases in section 4 are available at `https://github.com/glwagner/SingleColumnModelCalibration.jl`.

Acknowledgments

Our work is supported by the generosity of Eric and Wendy Schmidt by recommendation of the Schmidt Futures program and by NSF grant AGS-1835576. N.C.C. is supported by the Australian Research Council DECRA Fellowship DE210100749.

References

Belcher, S. E., Grant, A. L., Hanley, K. E., Fox-Kemper, B., Van Roekel, L., Sullivan, P. P., ... others (2012). A global perspective on langmuir turbulence in the ocean surface boundary layer. *Geophysical Research Letters*, *39*(18).

Blanke, B., & Delecluse, P. (1993). Variability of the tropical Atlantic Ocean simulated by a general circulation model with two different mixed-layer physics. *Journal of Physical Oceanography*, *23*(7), 1363–1388.

Burchard, H., & Bolding, K. (2001). Comparative analysis of four second-moment turbulence closure models for the oceanic mixed layer. *Journal of Physical Oceanography*, *31*(8), 1943–1968.

Colm-cille, P. C. (2020). Open questions in turbulent stratified mixing: do we even know what we do not know? *Physical Review Fluids*, *5*(11), 110518.

Deardorff, J. W., et al. (1970). Convective velocity and temperature scales for the unstable planetary boundary layer and for Rayleigh convection. *J. atmos. Sci*, *27*(8), 1211–1213.

Dunbar, O. R., Lopez-Gomez, I., Garbuno-Iñigo, A., Huang, D. Z., Bach, E., & Wu, J. (2022). EnsembleKalmanProcesses.jl: Derivative-free ensemble-based model calibration. *Journal of Open Source Software*, *7*(80), 4869. doi: 10.21105/joss.04869

Duraisamy, K. (2021). Perspectives on machine learning-augmented Reynolds-averaged and large eddy simulation models of turbulence. *Physical Review Fluids*, *6*(5), 050504.

DuVivier, A. K., Large, W. G., & Small, R. J. (2018). Argo observations of the deep mixing band in the Southern Ocean: A salinity modeling challenge. *Journal of Geophysical Research: Oceans*, *123*(10), 7599–7617.

Frezat, H., Le Sommer, J., Fablet, R., Balarac, G., & Lguensat, R. (2022). A posteriori learning for quasi-geostrophic turbulence parametrization. *Journal of Advances in Modeling Earth Systems*, *14*(11).

Gaspar, P., Grégoris, Y., & Lefevre, J.-M. (1990). A simple eddy kinetic energy model for simulations of the oceanic vertical mixing: Tests at station Papa and long-term upper ocean study site. *Journal of Geophysical Research: Oceans*, *95*(C9), 16179–16193.

Gregg, M. C., D'Asaro, E. A., Riley, J. J., & Kunze, E. (2018). Mixing efficiency in the ocean. *Annual review of marine science*, *10*, 443–473.

Groeskamp, S., Griffies, S. M., Iudicone, D., Marsh, R., Nurser, A. G., & Zika, J. D. (2019). The water mass transformation framework for ocean physics and biogeochemistry. *Annual review of marine science*, *11*, 271–305.

Gutjahr, O., Brüggemann, N., Haak, H., Jungclaus, J. H., Putrasahan, D. A., Lohmann, K., & von Storch, J.-S. (2021). Comparison of ocean vertical mixing schemes in the Max Planck Institute Earth System Model (MPI-ESM1. 2). *Geoscientific Model Development*, *14*(5), 2317–2349.

Häfner, D., Nuterman, R., & Jochum, M. (2021). Fast, cheap, and turbulent—global ocean modeling with gpu acceleration in python. *Journal of Advances in Modeling Earth Systems*, *13*(12), e2021MS002717.

Harcourt, R. R., & D'Asaro, E. A. (2008). Large-eddy simulation of Langmuir turbulence in pure wind seas. *Journal of Physical Oceanography*, *38*(7), 1542–1562.

Hughes, K. G., Moum, J. N., & Shroyer, E. L. (2020). Heat transport through diurnal warm layers. *Journal of Physical Oceanography*, *50*(10), 2885–2905.

Iglesias, M. A., Law, K. J., & Stuart, A. M. (2013). Ensemble Kalman methods for inverse problems. *Inverse Problems*, *29*(4), 045001.

Jackson, L., Hallberg, R., & Legg, S. (2008). A parameterization of shear-driven turbulence for ocean climate models. *Journal of Physical Oceanography*, *38*(5), 1033–1053.

Jungclaus, J. H., Lorenz, S. J., Schmidt, H., Brovkin, V., Brüggemann, N., Chegini, F., ... others (2022). The ICON earth system model version 1.0. *Journal of Advances in Modeling Earth Systems*, *14*(4), e2021MS002813.

Kuhlbrodt, T., Jones, C. G., Sellar, A., Storkey, D., Blockley, E., Stringer, M., ... others (2018). The low-resolution version of HadGEM3 GC3. 1: Development and evaluation for global climate. *Journal of Advances in Modeling Earth Systems*, *10*(11), 2865–2888.

Large, W. G., McWilliams, J. C., & Doney, S. C. (1994). Oceanic vertical mixing: A review and a model with a nonlocal boundary layer parameterization. *Reviews of geophysics*, *32*(4), 363–403.

Legg, S., Briegleb, B., Chang, Y., Chassignet, E. P., Danabasoglu, G., Ezer, T., ... others (2009). Improving oceanic overflow representation in climate models: the gravity current entrainment climate process team. *Bulletin of the American Meteorological Society*, *90*(5), 657–670.

Lenain, L., & Pizzo, N. (2020). The contribution of high-frequency wind-generated surface waves to the Stokes drift. *Journal of Physical Oceanography*, *50*(12), 3455–3465.

Li, D. (2019). Turbulent Prandtl number in the atmospheric boundary layer-where are we now? *Atmospheric Research*, *216*, 86–105.

Li, G., & Xie, S.-P. (2014). Tropical biases in CMIP5 multimodel ensemble: The excessive equatorial pacific cold tongue and double itcz problems. *Journal of Climate*, *27*(4), 1765–1780.

Luyten, J., Pedlosky, J., & Stommel, H. (1983). The ventilated thermocline. *Journal of Physical Oceanography*, *13*(2), 292–309.

Madec, G., Bourdallé-Badie, R., Bouttier, P.-A., Bricaud, C., Bruciaferri, D., Calvert, D., ... others (2017). NEMO ocean engine.

McDougall, T. J., & Barker, P. M. (2011). Getting started with TEOS-10 and the Gibbs Seawater (GSW) oceanographic toolbox. *Scor/Iapso WG*, *127*, 1–28.

McWilliams, J. C., Huckle, E., & Shchepetkin, A. F. (2009). Buoyancy effects in a stratified ekman layer. *Journal of Physical Oceanography*, *39*(10), 2581–2599.

Mellor, G. L., & Yamada, T. (1982). Development of a turbulence closure model for geophysical fluid problems. *Reviews of Geophysics*, *20*(4), 851–875.

Moulin, A. J., Moum, J. N., & Shroyer, E. L. (2018). Evolution of turbulence in the diurnal warm layer. *Journal of Physical Oceanography*, *48*(2), 383–396.

Omand, M. M., D'Asaro, E. A., Lee, C. M., Perry, M. J., Briggs, N., Cetinić, I., & Mahadevan, A. (2015). Eddy-driven subduction exports particulate organic carbon from the spring bloom. *Science*, *348*(6231), 222–225.

Osborn, T. (1980). Estimates of the local rate of vertical diffusion from dissipation measurements. *Journal of physical oceanography*, *10*(1), 83–89.

Prandtl, L., Wieselsberger, C., & Betz, A. (1925). *Results of the aerodynamic research institute in göttingen* (No. 1). R. Oldenburg.

Price, J. F., Weller, R. A., & Pinkel, R. (1986). Diurnal cycling: Observations and models of the upper ocean response to diurnal heating, cooling, and wind mixing. *Journal of Geophysical Research: Oceans*, *91*(C7), 8411–8427.

Ramadhan, A., Marshall, J. C., Souza, A. N., Lee, X. K., Piterbarg, U., Hillier, A., ... Ferrari, R. (2022). Capturing missing physics in climate model parameterizations using neural differential equations. *Earth and Space Science Open Archive*, 67. doi: 10.1002/essoar.10512533.1

Ramadhan, A., Wagner, G. L., Hill, C., Campin, J.-M., Churavy, V., Besard, T., ... Ferrari, R. (2020). Oceananigans.jl: Fast and friendly geophysical fluid dynamics on GPUs. *The Journal of Open Source Software*, *4*(44), 1965. doi: 10.21105/joss.01965

Reffray, G., Bourdalle-Badie, R., & Calone, C. (2015). Modelling turbulent vertical mixing sensitivity using a 1-D version of NEMO. *Geoscientific Model Development*, *8*(1), 69–86.

Reichl, B. G., & Hallberg, R. (2018). A simplified energetics based planetary boundary layer (ePBL) approach for ocean climate simulations. *Ocean Modelling*, *132*, 112–129.

Reichl, B. G., & Li, Q. (2019). A parameterization with a constrained potential energy conversion rate of vertical mixing due to Langmuir turbulence. *Journal of Physical Oceanography*, *49*(11), 2935–2959.

Saffman, P. G. (1970). A model for inhomogeneous turbulent flow. *Proceedings of the Royal Society of London. A. Mathematical and Physical Sciences*, *317*(1530), 417–433.

Sallée, J.-B., Shuckburgh, E., Bruneau, N., Meijers, A. J., Bracegirdle, T. J., & Wang, Z. (2013). Assessment of Southern Ocean mixed-layer depths in CMIP5 models: Historical bias and forcing response. *Journal of Geophysical Research: Oceans*, *118*(4), 1845–1862.

Sarkar, S., & Pham, H. T. (2019). Turbulence and thermal structure in the upper ocean: Turbulence-resolving simulations. *Flow, Turbulence and Combustion*, *103*, 985–1009.

Siebesma, A. P., Soares, P. M., & Teixeira, J. (2007). A combined eddy-diffusivity mass-flux approach for the convective boundary layer. *Journal of the atmospheric sciences*, *64*(4), 1230–1248.

Smith, K. M., Caulfield, C., & Taylor, J. (2021). Turbulence in forced stratified shear flows. *Journal of Fluid Mechanics*, *910*, A42.

Smyth, W., & Moum, J. (2013). Marginal instability and deep cycle turbulence in the eastern equatorial pacific ocean. *Geophysical Research Letters*, *40*(23), 6181–6185.

Souza, A., He, J., Bischoff, T., Waruszewski, M., Novak, L., Barra, V., ... others (2022). The flux-differencing discontinuous galerkin method applied to an idealized fully compressible nonhydrostatic dry atmosphere. *Authorea Preprints*.

Souza, A., Wagner, G., Ramadhan, A., Allen, B., Churavy, V., Schloss, J., ... others (2020). Uncertainty quantification of ocean parameterizations: Application to the K-profile-parameterization for penetrative convection. *Journal of Advances in Modeling Earth Systems*, *12*(12), e2020MS002108.

Spalding, D. B. (1991). Kolmogorov's two-equation model of turbulence. *Proceedings of the Royal Society of London. Series A: Mathematical and Physical Sciences*, *434*(1890), 211–216.

Umlauf, L., & Burchard, H. (2003). A generic length-scale equation for geophysical turbulence models. *Journal of Marine Research*, *61*(2), 235–265.

Van Roekel, L., Adcroft, A. J., Danabasoglu, G., Griffies, S. M., Kauffman, B., Large, W., ... Schmidt, M. (2018). The KPP boundary layer scheme for the ocean: Revisiting its formulation and benchmarking one-dimensional simulations relative to LES. *Journal*

of Advances in Modeling Earth Systems, *10*(11), 2647–2685.

Wagner, G. L., Hillier, A., & Constantinou, N. C. (2022). *ParameterEstimocean.jl v0.14.2: Julia package for parameter estimation of turbulence closures for ocean models using Ensemble Kalman Inversion.* doi: 10.5281/zenodo.5762810

Wagner, G. L., Ramadhan, A., Chor, T., Constantinou, N. C., Hillier, A., Lee, X. K., & Li, Q. (2023). *LESbrary.jl: v0.1.1: Oceananigans large eddy simulation (LES) data for calibrating parameterizations.* (doi:10.5281/zenodo.7997002) doi: 10.5281/zenodo.7997002

Whitt, D., Cherian, D., Holmes, R., Bachman, S., Lien, R.-C., Large, W., & Moum, J. (2022). Simulation and scaling of the turbulent vertical heat transport and deep-cycle turbulence across the equatorial Pacific cold tongue. *Journal of Physical Oceanography*, *52*(5), 981–1014.

Williams, R. G. (1991). The role of the mixed layer in setting the potential vorticity of the main thermocline. *Journal of Physical Oceanography*, *21*(12), 1803–1814.

Zhang, S., Fu, H., Wu, L., Li, Y., Wang, H., Zeng, Y., ... others (2020). Optimizing high-resolution community earth system model on a heterogeneous many-core supercomputing platform. *Geoscientific Model Development*, *13*(10), 4809–4829.

Figure 1.

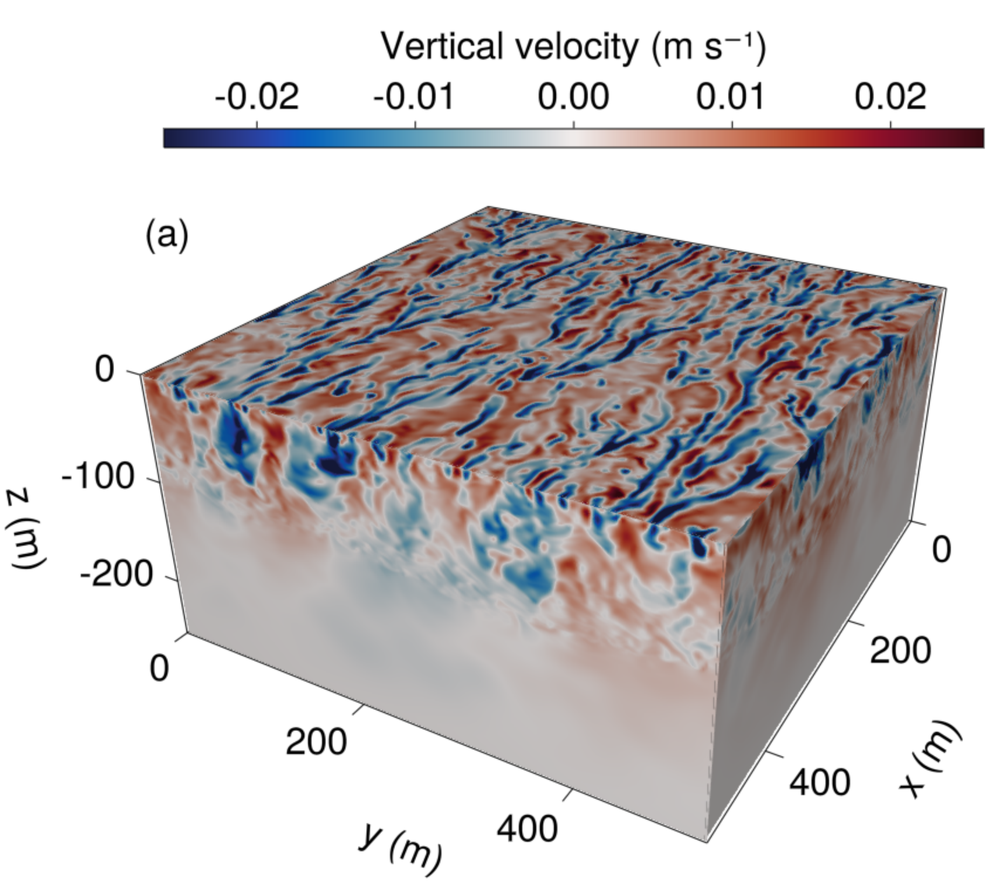
Vertical velocity (m s⁻¹)
-0.02
-0.01
0.00
0.01
0.02
(a)
z (m)
0
-100
-200
0
200
400
y (m)
0
200
400
x (m)

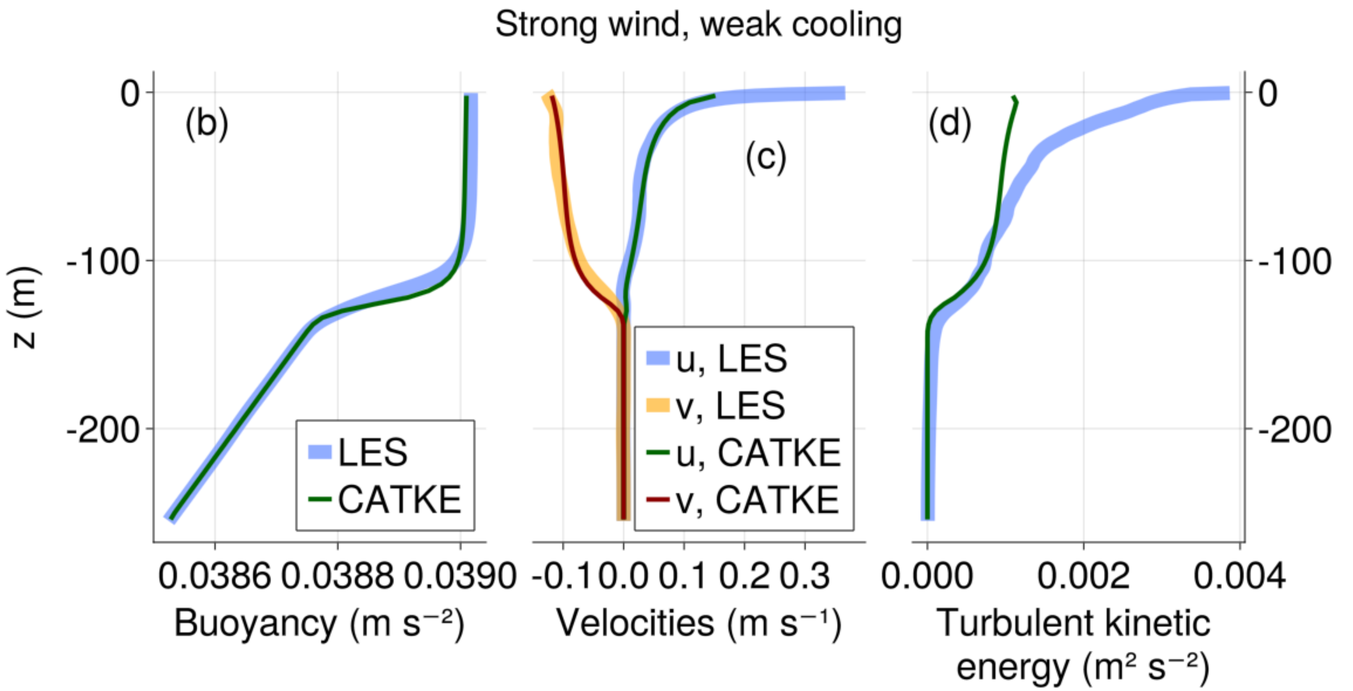
Strong wind, weak cooling
(b)
(c)
(d)
z (m)
0
-100
-200
LES
CATKE
u, LES
v, LES
u, CATKE
v, CATKE
0.0386 0.0388 0.0390
Buoyancy (m s⁻²)
-0.1 0.0 0.1 0.2 0.3
Velocities (m s⁻¹)
0.000
0.002
0.004
Turbulent kinetic energy (m² s⁻²)

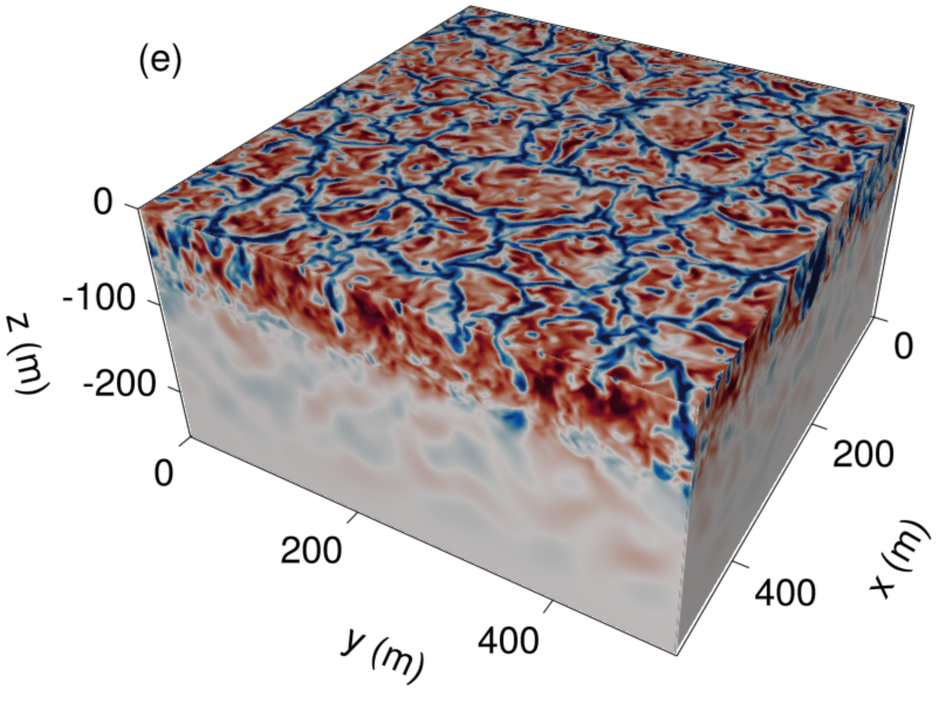
(e)
z (m)
0
-100
-200
0
200
400
y (m)
0
200
400
x (m)

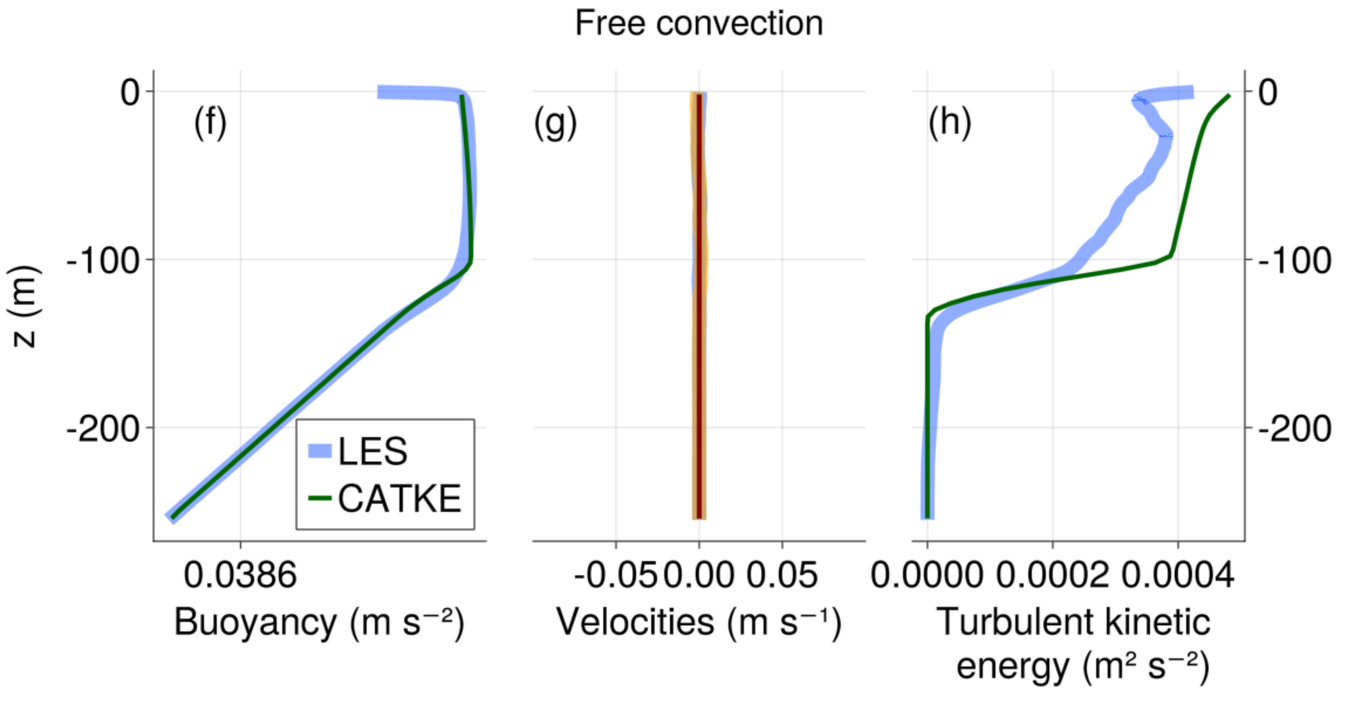
Free convection
(f)
(g)
(h)
z (m)
0
-100
-200
LES
CATKE
0.0386
Buoyancy (m s⁻²)
-0.05 0.00 0.05
Velocities (m s⁻¹)
0.0000 0.0002 0.0004
Turbulent kinetic energy (m² s⁻²)

Figure 2.

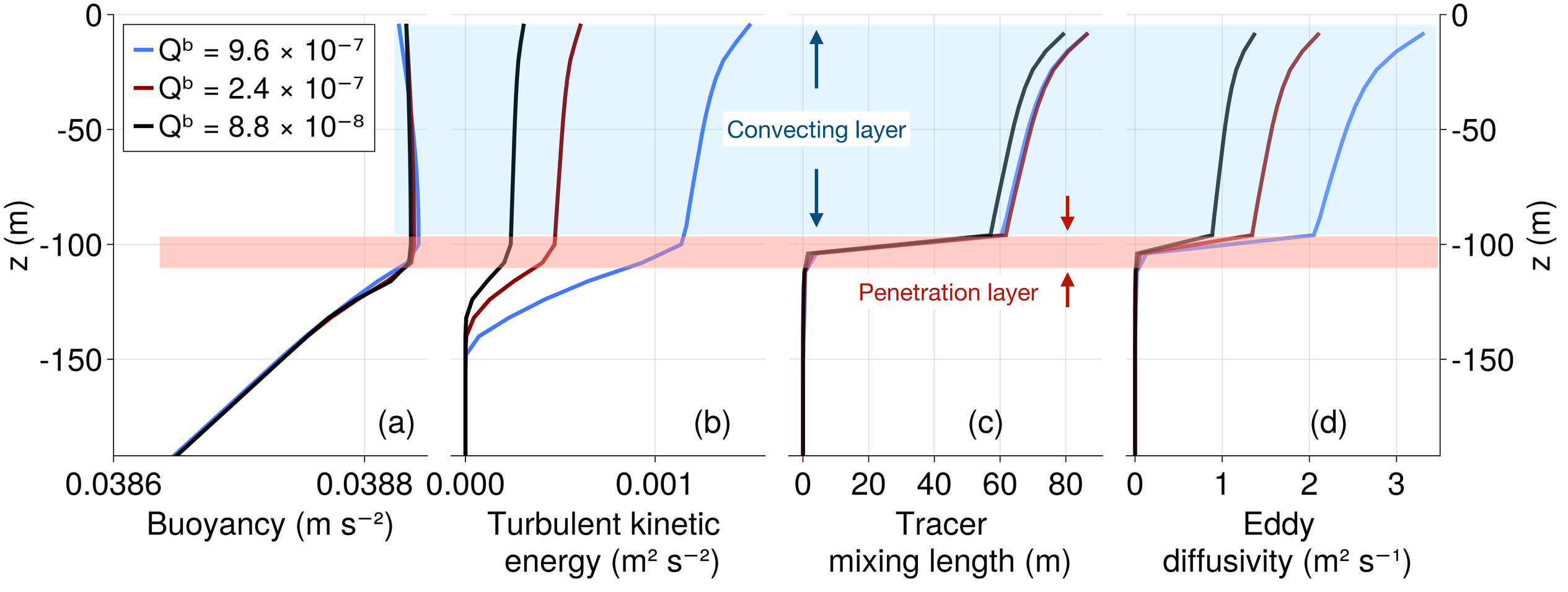
$Q^b = 9.6 \times 10^{-7}$
$Q^b = 2.4 \times 10^{-7}$
$Q^b = 8.8 \times 10^{-8}$
Convecting layer
Penetration layer
z (m)
0
-50
-100
-150
(a)
(b)
(c)
(d)
0.0386
0.0388
Buoyancy (m s^{-2})
0.000
0.001
Turbulent kinetic energy (m^2 s^{-2})
0
20
40
60
80
Tracer mixing length (m)
0
1
2
3
Eddy diffusivity (m^2 s^{-1})

Figure 3.

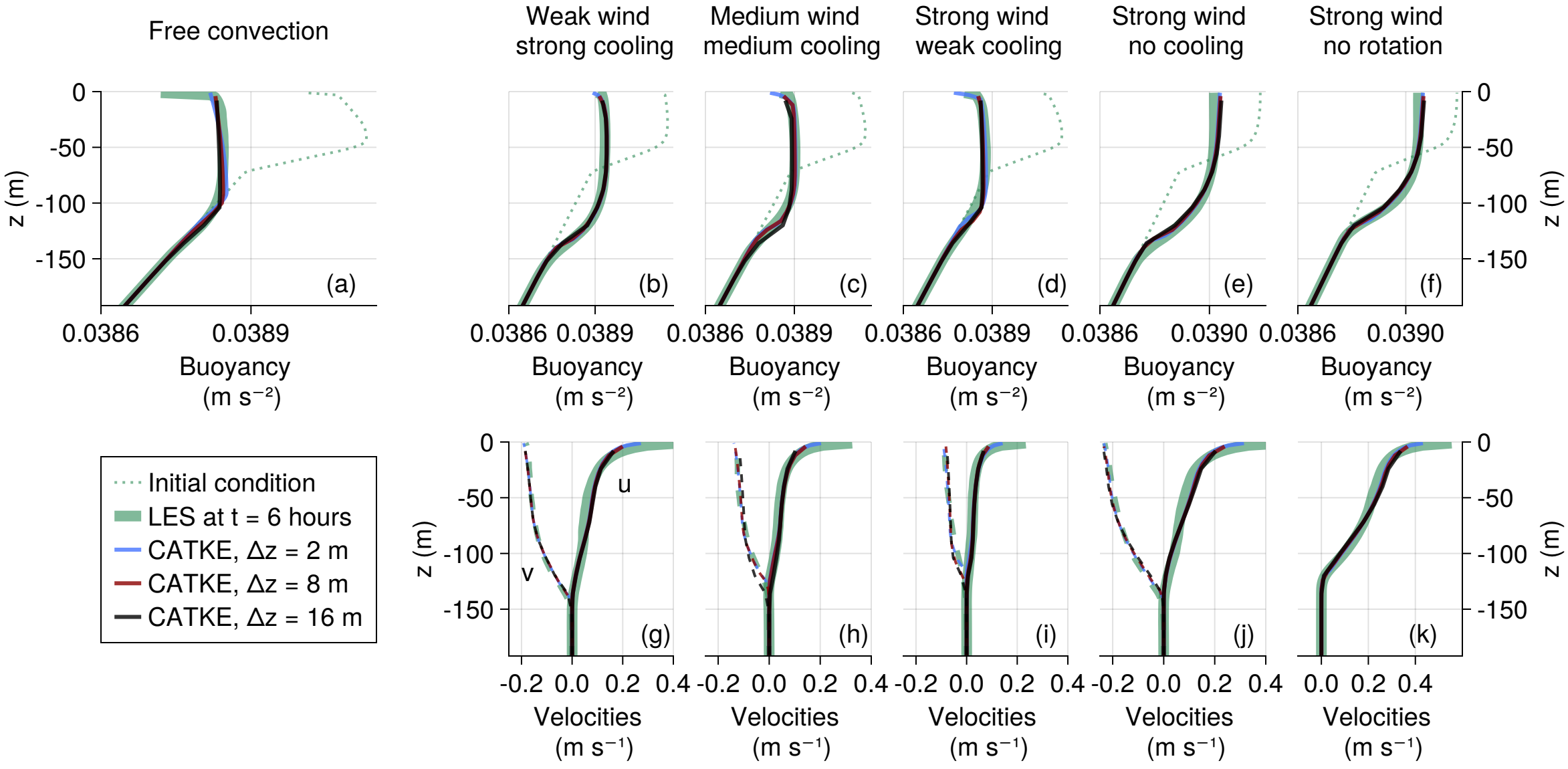
Free convection
Weak wind
strong cooling
Medium wind
medium cooling
Strong wind
weak cooling
Strong wind
no cooling
Strong wind
no rotation
z (m)
0
-50
-100
-150
(a)
(b)
(c)
(d)
(e)
(f)
0.0386
0.0389
0.0390
Buoyancy
(m s⁻²)
Initial condition
LES at t = 6 hours
CATKE, Δz = 2 m
CATKE, Δz = 8 m
CATKE, Δz = 16 m
u
v
(g)
(h)
(i)
(j)
(k)
-0.2
0.0
0.2
0.4
Velocities
(m s⁻¹)

Figure 4.

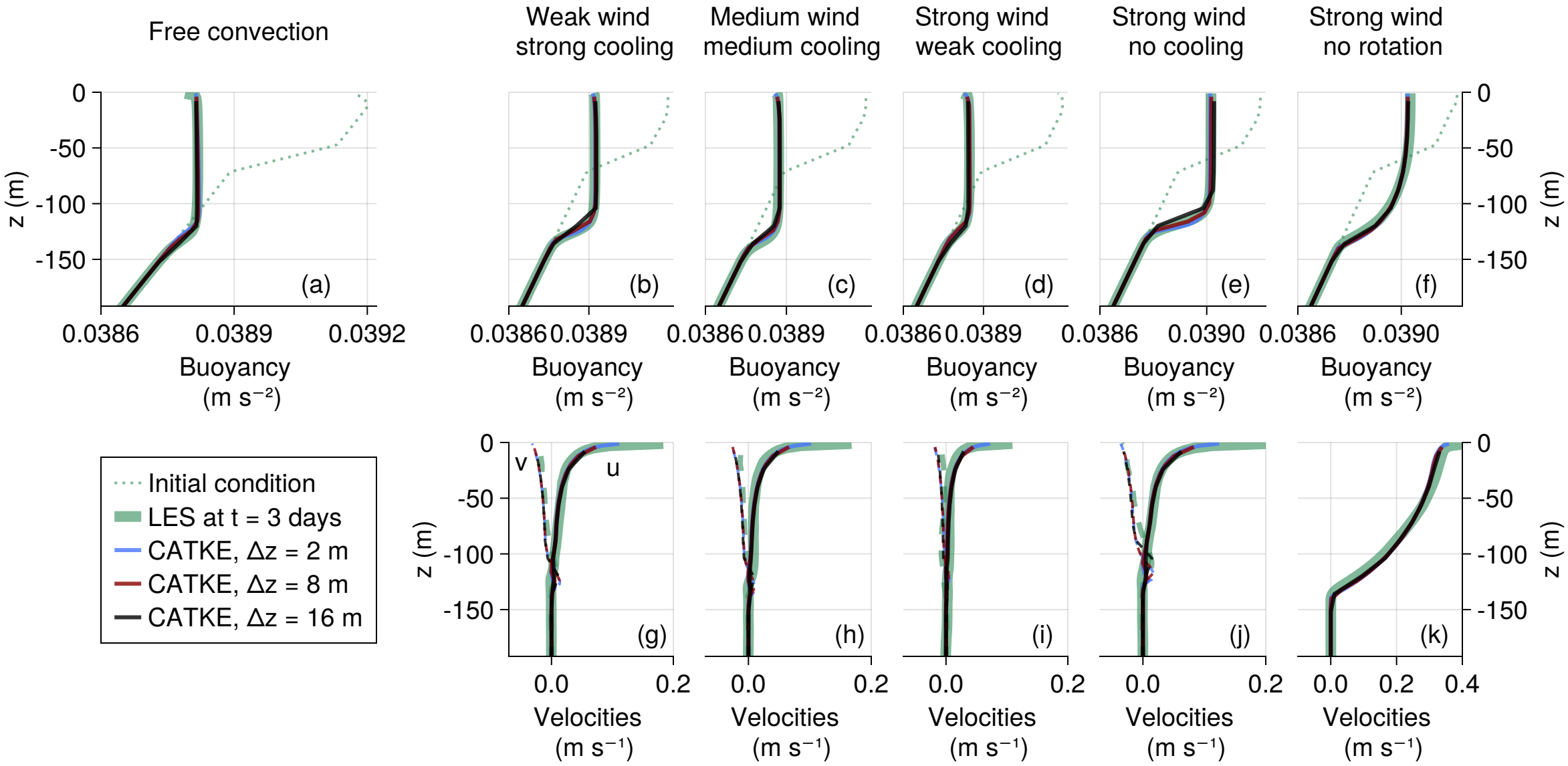
Free convection
Weak wind
strong cooling
Medium wind
medium cooling
Strong wind
weak cooling
Strong wind
no cooling
Strong wind
no rotation
z (m)
0
-50
-100
-150
(a)
(b)
(c)
(d)
(e)
(f)
0.0386
0.0389
0.0392
0.0390
Buoyancy
(m s⁻²)
Initial condition
LES at t = 3 days
CATKE, Δz = 2 m
CATKE, Δz = 8 m
CATKE, Δz = 16 m
v
u
(g)
(h)
(i)
(j)
(k)
0.0
0.2
0.4
Velocities
(m s⁻¹)

Figure 5.

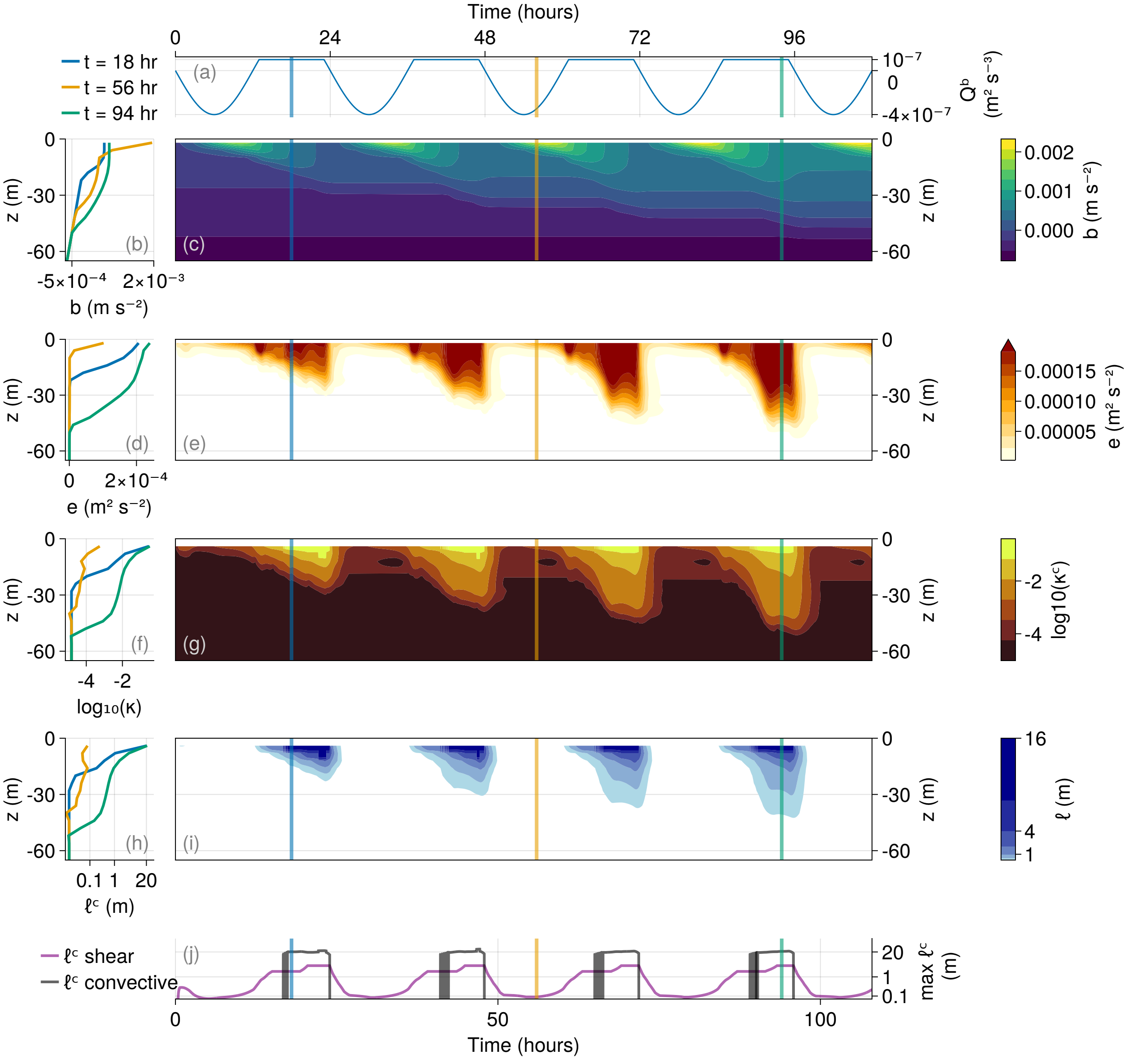
Time (hours)
0
24
48
72
96
t = 18 hr
t = 56 hr
t = 94 hr
(a)
10^{-7}
0
-4×10^{-7}
Q^b ($m^2\ s^{-3}$)
z (m)
0
-30
-60
(b)
(c)
-5×10^{-4}
2×10^{-3}
b ($m\ s^{-2}$)
0.002
0.001
0.000
b ($m\ s^{-2}$)
(d)
(e)
0
2×10^{-4}
e ($m^2\ s^{-2}$)
0.00015
0.00010
0.00005
e ($m^2\ s^{-2}$)
(f)
(g)
-4
-2
$\log_{10}(\kappa)$
-2
-4
$\log10(\kappa^c)$
(h)
(i)
0.1
1
20
ℓ^c (m)
16
4
1
ℓ (m)
ℓ^c shear
ℓ^c convective
(j)
20
1
0.1
max ℓ^c (m)
0
50
100
Time (hours)

Figure 6.

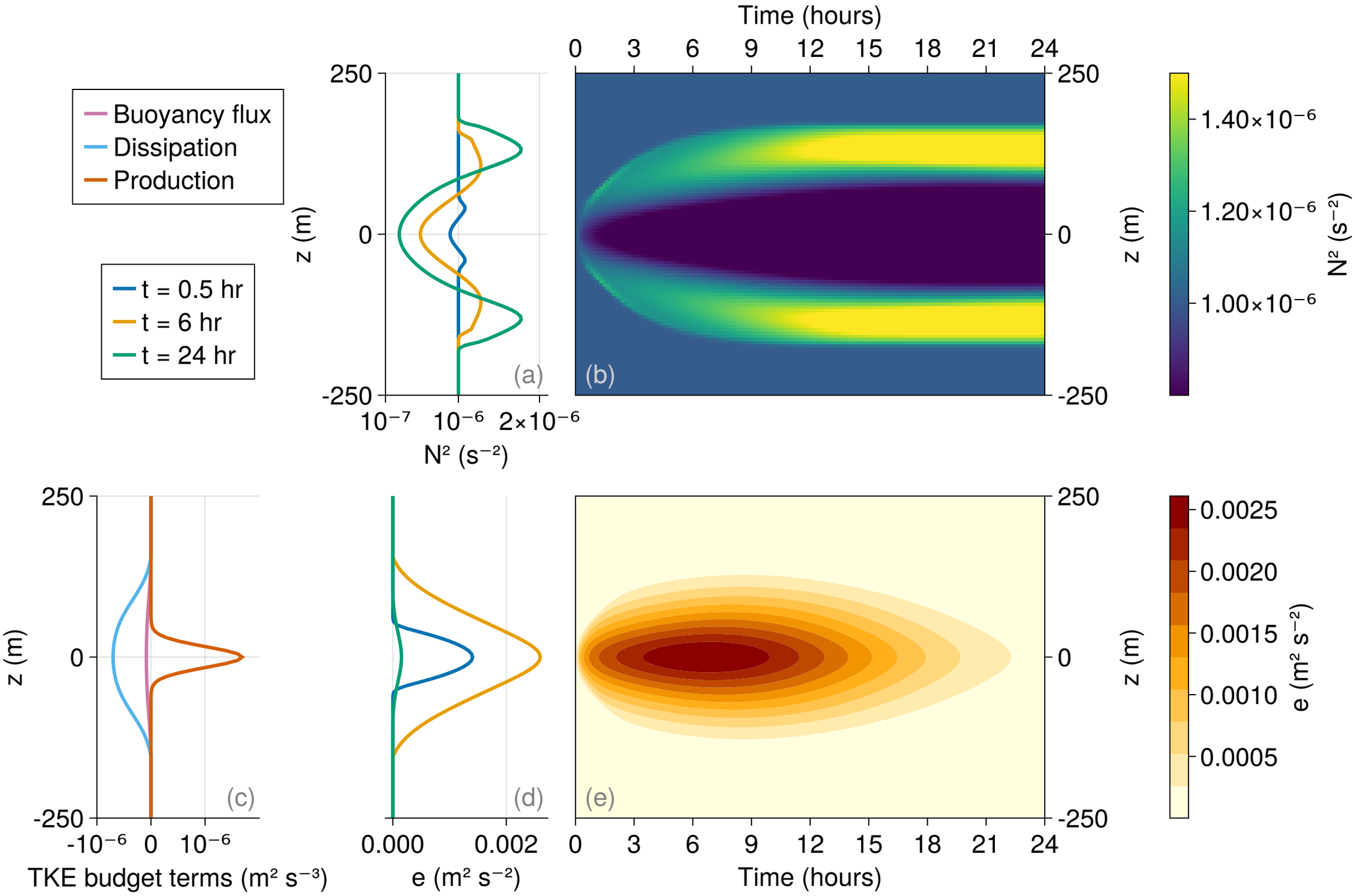
Buoyancy flux
Dissipation
Production
t = 0.5 hr
t = 6 hr
t = 24 hr
z (m)
250
0
-250
10⁻⁷
10⁻⁶
2×10⁻⁶
N² (s⁻²)
(a)
Time (hours)
0
3
6
9
12
15
18
21
24
(b)
1.40×10⁻⁶
1.20×10⁻⁶
1.00×10⁻⁶
N² (s⁻²)
-10⁻⁶
10⁻⁶
TKE budget terms (m² s⁻³)
(c)
0.000
0.002
e (m² s⁻²)
(d)
(e)
0.0025
0.0020
0.0015
0.0010
0.0005
e (m² s⁻²)

Figure 7.

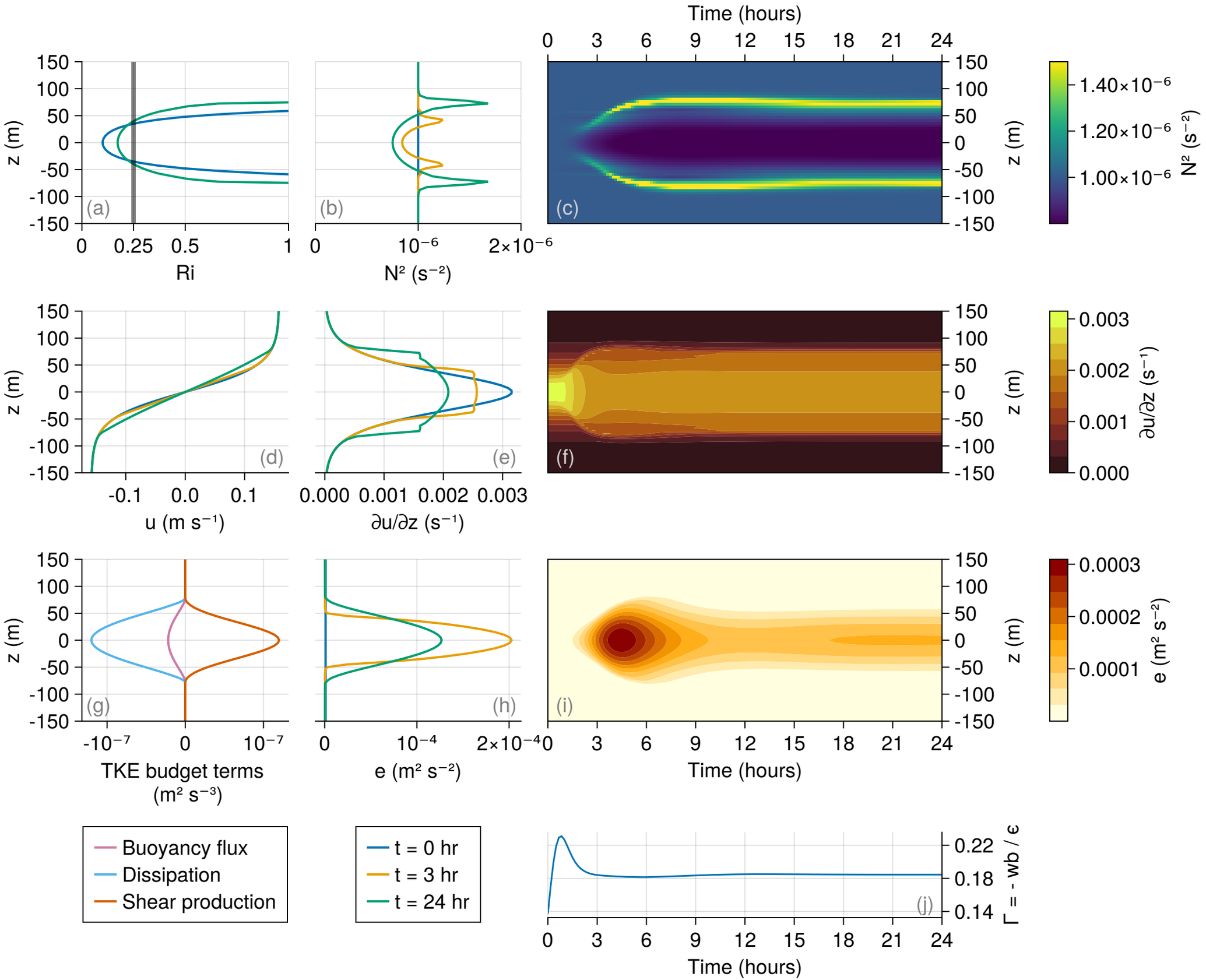
Time (hours)
z (m)
Ri
N² (s⁻²)
u (m s⁻¹)
∂u/∂z (s⁻¹)
TKE budget terms
(m² s⁻³)
e (m² s⁻²)
Γ = - wb / ϵ
(a)
(b)
(c)
(d)
(e)
(f)
(g)
(h)
(i)
(j)
Buoyancy flux
Dissipation
Shear production
t = 0 hr
t = 3 hr
t = 24 hr

Figure 8.

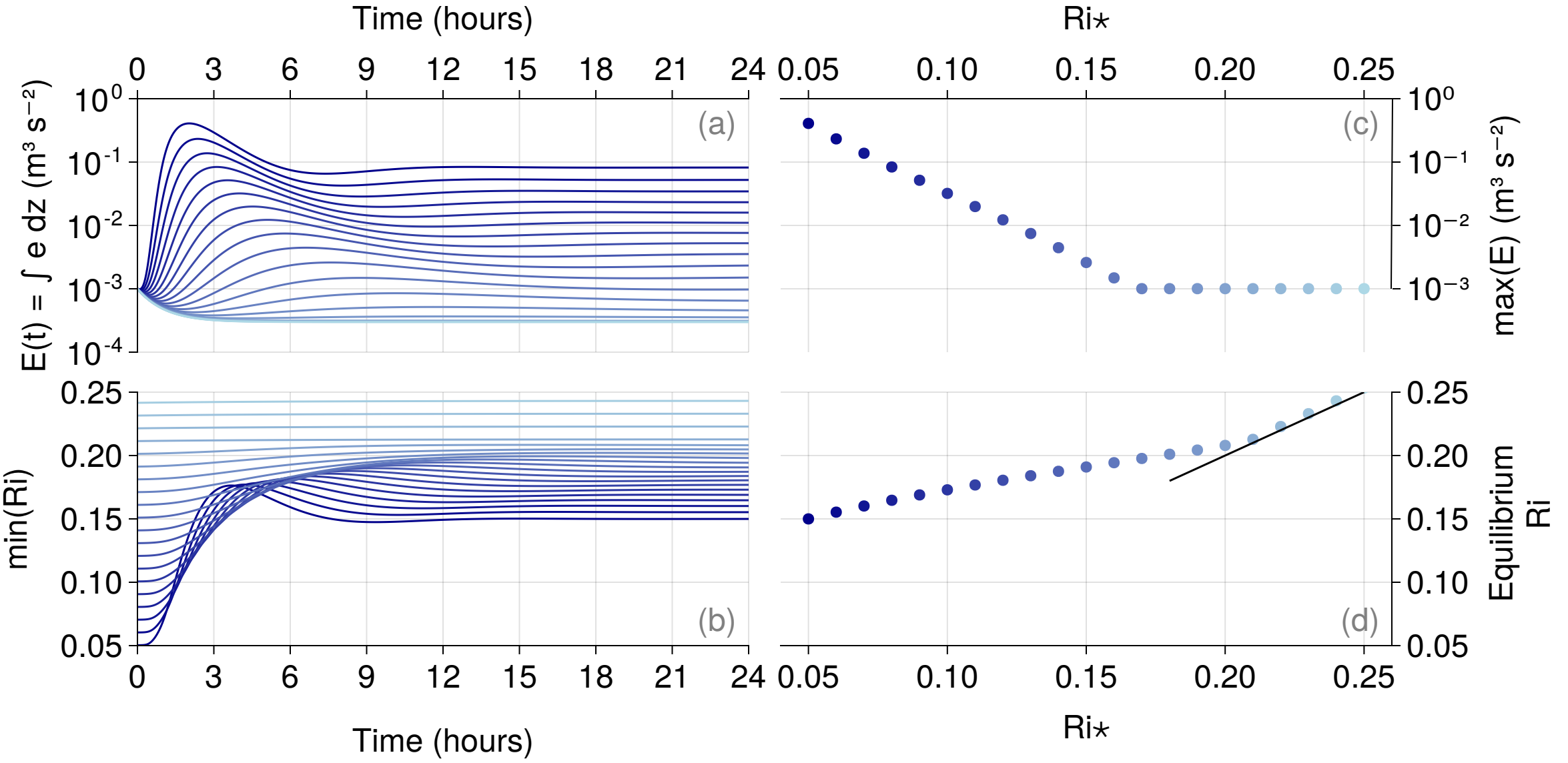
Time (hours)
0
3
6
9
12
15
18
21
24
10^{0}
10^{-1}
10^{-2}
10^{-3}
10^{-4}
E(t) = ∫ e dz (m³ s⁻²)
(a)
0.25
0.20
0.15
0.10
0.05
min(Ri)
(b)
Time (hours)
Ri⋆
0.05
0.10
0.15
0.20
0.25
(c)
max(E) (m³ s⁻²)
(d)
Equilibrium Ri
Ri⋆